The Astrophysical Journal Supplement Series, 238:14 (25pp), 2018 October https://doi.org/10.3847/1538-4365/aad81a

The 21-SPONGE H I Absorption Line Survey. I. The Temperature of Galactic H I

Claire E. Murray[1,2], Snežana Stanimirović[1], W. M. Goss[3], Carl Heiles[4], John M. Dickey[5], Brian Babler[1], and Chang-Goo Kim[6,7]

[1] Department of Astronomy, University of Wisconsin, Madison, WI 53706, USA; clairemurray56@gmail.com
[2] Space Telescope Science Institute, 3700 San Martin Drive, Baltimore, MD 21218, USA
[3] National Radio Astronomy Observatory, P.O. Box O, 1003 Lopezville, Socorro, NM 87801, USA
[4] Radio Astronomy Lab, University of California, Berkeley, 601 Campbell Hall, Berkeley CA 94720, USA
[5] University of Tasmania, School of Maths and Physics, Hobart, TAS 7001, Australia
[6] Department of Astrophysical Sciences, Princeton University, Princeton, NJ 08544, USA
[7] Center for Computational Astrophysics, Flatiron Institute, New York, NY 10010, USA
Received 2018 June 2; revised 2018 August 2; accepted 2018 August 3; published 2018 September 27

Abstract

We present 21 cm Spectral Line Observations of Neutral Gas with the VLA (21-SPONGE), a Karl G. Jansky Very Large Array (VLA) large project (∼600 hr) for measuring the physical properties of Galactic neutral hydrogen (H I). 21-SPONGE is distinguished among previous Galactic H I studies as a result of (1) its exceptional optical depth sensitivity ($\sigma_\tau < 10^{-3}$ per 0.42 km s^{-1} channel over 57 lines of sight), (2) matching 21 cm emission spectra with the highest possible angular resolution (∼4′) from the Arecibo Observatory, and (3) detailed comparisons with numerical simulations for assessing observational biases. We autonomously decompose 21 cm spectra and derive the physical properties (i.e., spin temperature, T_s, and column density) of the cold neutral medium (CNM; $T_s < 250$ K), thermally unstable medium (UNM; 250 K $< T_s <$ 1000 K), and warm neutral medium (WNM; $T_s > 1000$ K) simultaneously. Of the total H I mass observed, 50% is detected in both absorption and emission. The CNM makes up the majority of the absorbing gas (56% ± 10%) and 28% of the total H I mass including gas detected only in emission. We find that 20% of the total H I mass is thermally unstable (41% ± 10% of H I detected in absorption), with no significant variation with Galactic latitude. Finally, although the WNM makes up 52% of the total H I mass, we detect little evidence for WNM absorption with 1000 K $< T_s <$ 4000 K. Following spectral modeling, we detect a stacked residual absorption feature corresponding to WNM with $T_s \sim 10^4$ K. We conclude that excitation in excess of collisions likely produces significantly higher WNM T_s than predicted by steady-state models.

Key words: ISM: clouds – ISM: structure – radio lines: ISM

Supporting material: figure sets

1. Introduction

The formation of stars and the evolution of galaxies rely on the cycle of interstellar matter (ISM) between supernova-expelled plasma and molecule-rich gas. At the center of this cycle is neutral hydrogen (H I), the fundamental fuel for star-forming clouds whose physical conditions comprise key constraints for theoretical models.

Following the first astronomical observations of absorption and emission via the 21 cm transition of H I (Ewen & Purcell 1951; Muller & Oort 1951; Hagen et al. 1955), clear differences in the observed velocity structure between 21 cm emission and absorption were attributed to significant variations in the temperature and density of the gas along the line of sight (LOS; e.g., Clark 1965; Dickey et al. 1978). Theoretical models of steady-state ISM heating and cooling quantified the nature of this thermal phase structure, predicting two thermally stable phases: the cold neutral medium (CNM) and warm neutral medium (WNM), with density and kinetic temperatures of (n, T_k) = (7–70 cm^{-3}, 60–260 K), and (n, T_k) = (0.2–0.9 cm^{-3}, 5000–8300 K), respectively (McKee & Ostriker 1977; Wolfire et al. 2003). However, subsequent analytical models and numerical simulations determined that time-dependent or dynamical processes such as turbulence and supernova shocks are likely very important and will generate a significant amount of thermally unstable gas (UNM) in the intervening parameter space between CNM and WNM, thus throwing into question the validity of the steady-state paradigm of the ISM (e.g., Dalgarno & McCray 1972; Vázquez-Semadeni et al. 2000; Audit & Hennebelle 2005).

However, the physical properties, mass fractions, and ionization state of the diffuse neutral gas phases (i.e., WNM and UNM) are particularly sensitive to macro- and micro-physical heating and cooling processes (Heiles & Troland 2003b). These include magnetic wave dissipation (e.g., Ferrière et al. 1988), magnetic reconnection (e.g., Vishniac & Lazarian 1999), turbulence (e.g., Audit & Hennebelle 2005), supernovae (e.g., Mac Low et al. 2005), diffusion of photons from H II regions, and diffusion of low-energy cosmic rays and X-rays from time-dependent stellar phenomena. As these processes originate from sources on a huge range of physical and temporal scales, understanding them as part of a self-consistent model of the ISM has proven challenging.

Furthermore, observational constraints for the properties of the UNM and WNM have been historically limited by insufficient observational capabilities. To constrain the optical depth and excitation (or spin) temperature of H I—crucial for determining the thermodynamic state of the gas—measurements of both emission and absorption at 21 cm are necessary. Due to their low densities, detecting the absorbing properties of the WNM and UNM requires extremely high sensitivity to H I optical depth. For example, past observations of 21 cm

absorption with single-dish and interferometric telescopes were primarily sensitive to detecting absorption by the CNM with $T_s = 60$–80 K (Hughes et al. 1971; Radhakrishnan et al. 1972; Crovisier et al. 1978). Improved sensitivity to optical depth revealed absorption by H I with warmer temperatures, up to ~600 K (Lazareff 1975; Dickey et al. 1977). Only a handful of detections of WNM with $T_s \gtrsim 1000$ K exist (Carilli et al. 1998; Dwarakanath et al. 2002; Murray et al. 2015).

Considering the expense of high-sensitivity absorption measurements, and the fact that they are limited by the availability of sources of background continuum radiation, warm H I (i.e., UNM and WNM) properties are typically indirectly estimated from 21 cm emission alone. Kinetic temperatures inferred from the Gaussian line widths of decomposed 21 cm emission profiles indicate that a significant fraction of the H I mass is thermally unstable, with $T_s \sim 3000$ K (e.g., Verschuur & Magnani 1994; Haud & Kalberla 2007). For example, following the Gaussian decomposition of all-sky H I emission survey data from the Effelsberg–Bonn H I Survey (EBHIS; Winkel et al. 2016) and the Galactic All-Sky Survey (GASS; McClure-Griffiths et al. 2009; Kalberla et al. 2010; Kalberla & Haud 2015), Kalberla & Haud (2018) concluded that 41% of H I in the local ISM ($|v_{\rm LSR}| < 8$ km s^{-1}) is in the "lukewarm" (a.k.a. thermally unstable) medium. The Millennium Arecibo 21 cm Absorption-Line Survey detected absorption from gas with excitation temperatures of ~10–600 K and inferred that ~48% of the remaining material detected only in emission (i.e., ~30% of the total column density) is thermally unstable (Heiles & Troiland 2003b). From a high-sensitivity survey of 21 cm absorption toward 35 sources, Roy et al. 2013b estimated that at least 28% of H I is unstable. However, this result is based on H I emission data from the Leiden Argentine Bonn (LAB; Kalberla et al. 2005) survey, whose 36′ resolution probes much larger scales and thus different H I populations than their sub-arcminute interferometric absorption measurements.

Improving on previous observational efforts to constrain the physical properties of the diffuse H I, including the UNM mass fraction, requires expanded samples of 21 cm absorption lines at high sensitivity and careful attention to systematic uncertainties in analysis techniques.

1.1. The 21-SPONGE Survey

In this paper, we present the final data products from the largest survey for Galactic H I absorption to date at the Karl G. Jansky Very Large Array (VLA), titled 21 cm Observations of Neutral Gas with the (E)VLA (21-SPONGE). With superb sensitivity to 21 cm absorption, in combination with 21 cm emission from the Arecibo Observatory, 21-SPONGE is sensitive to CNM, UNM, and WNM temperatures and densities in the Galactic ISM. In Murray et al. (2015, hereafter M15), we presented the observation and data analysis strategies for 21-SPONGE, as well as preliminary analysis of 21 cm spectral line pairs. We demonstrated that the exceptional optical depth sensitivity of 21-SPONGE ($\sigma_\tau < 0.001$ per 0.42 km s^{-1} channel) enables direct detections of H I spin temperatures higher than previous observational studies by more than a factor of 2 (e.g., HT03).

Following the first half of the 21-SPONGE survey, we detected little evidence for WNM with $T_s > 1000$ K (<10% by number; M15). To improve sensitivity to shallow, broad absorption features further, we adapted a spectral stacking method to Galactic H I spectral line pairs and detected a pervasive population of WNM gas with $T_s = 7200^{+1800}_{-1200}$ K (Murray et al. 2014). This excitation temperature is significantly higher than predictions from standard ISM models based on collisional H I excitation (e.g., Liszt 2001) and suggests that additional excitation mechanisms such as resonant Lyα scattering (i.e., the Wouthuysen–Field (WF) effect; Wouthuysen 1952; Field 1958) are important for determining the thermodynamic properties of diffuse, neutral gas. Furthermore, enhanced 21 cm excitation has important implications for understanding H I signals from early epochs of cosmic time when H I dominated the baryonic content of the universe (Pritchard & Loeb 2012).

With the full 21-SPONGE survey now complete, our goal is to measure the mass distribution of H I as a function of temperature in the Galactic ISM. To prepare for this effort, in Murray et al. (2017) we considered the biases imposed by our analysis techniques in detail. Specifically, we analyzed synthetic H I absorption and emission spectral lines from a high-resolution, three-dimensional hydrodynamical simulation (Kim et al. 2013, 2014, hereafter KOK13 and KOK14) to assess the power of our observational methods for revealing the inherent state of the ISM. For the first time, we computed the completeness of H I structure recovery by Gaussian spectral line features and quantified the decline in completeness with latitude due to velocity crowding. Furthermore, we showed that the physical gas properties inferred from 21 cm spectral lines agree with the "true" simulated values within a factor of <2 for the majority of gas structures. We also identified a population of synthetic spectral features in KOK14, which are inconsistent with the properties of 21 cm spectra from 21-SPONGE, motivating improved treatment of H I excitation and feedback from star formation (Murray et al. 2017).

In this work, we will compare gas properties inferred from the KOK14 synthetic spectra to underlying physical properties of the KOK13 simulation to estimate the bias imposed by our spectral analysis methods on the overall mass distribution of H I as a function of temperature. Whereas in Murray et al. (2017) we focused on a subset of the KOK13 simulation—considering individual gas structures selected along simulated LOSs and how their inherent properties were recovered by individual spectral line features—in this work, we consider all gas along each simulated LOS. We will then use these comparisons to estimate uncertainties in the observed 21-SPONGE distribution to produce new constraints on the mass distribution of H I as a function of temperature.

This paper is organized as follows. In Section 2, we discuss the 21-SPONGE observations and synthetic data products used in our analysis. In Section 3, we discuss our revised Gaussian decomposition and radiative transfer approach, derived from HT03 and Murray et al. (2017). In Section 4, we present the results of our analysis of 21-SPONGE, including comparison with synthetic spectra from KOK14. In Section 6, we discuss these results, and we summarize our conclusions in Section 7.

2. Data

2.1. VLA 21 cm Absorption Spectra

The observing strategy for the 21-SPONGE H I absorption is described in M15 and summarized here for clarity. Our targets are bright ($S_{1.4\rm GHz} > 3$ Jy), radio continuum sources from the NRAO/VLA Sky Survey (NVSS; Condon et al. 1998) at high

Galactic latitude (most at $|b| > 10°$, with a sample at low latitude for comparison) with compact angular sizes ($<1'$) to minimize the complexity of the observed H I profiles and to avoid resolving substantial continuum flux.

For all VLA observations, we used three separate 500 kHz bands with 1.95 kHz channel spacing centered on the H I line (1.42040575 GHz) and ±1.5 MHz, respectively. We used the offline bands to avoid strong H I lines at Galactic velocities in the directions of our calibrator sources and to perform bandpass calibration via frequency switching. Bandpass calibration is of particular importance for 21-SPONGE, as our primary interest is to detect broad, shallow absorption lines associated with high-temperature H I. For details on our bandpass calibration strategies, we refer the reader to Section 2.2 of M15.

We reduced all 21-SPONGE data using the Astronomical Image Processing System (AIPS[8]; Greisen 2003). For a full description of the data reduction strategy, please see Section 2 of M15. For each source, we produce a cleaned, calibrated data cube and continuum image. We then extract the absorption spectrum from the pixel of maximum flux density and divide by the continuum flux density at the pixel location to compute $\exp(-\tau(v))$. Our channel spacing of 1.95 kHz at the H I frequency (0.42 km s^{-1} channel spacing in velocity) corresponds to a velocity resolution of 0.5 km s^{-1} (Rohlfs & Wilson 2004).

Of the original 58 target sources from the 21-SPONGE observing program,[9] 10 were removed upon inspection of preliminary data products for being overly resolved (three sources), displaying saturated absorption (two sources), or for not receiving integration time following the conclusion of the observing program (five sources). An additional nine sources were resolved into multiple continuum peaks, thereby providing additional sources for extracting H I absorption, albeit at degraded sensitivity due to the loss of continuum flux density. A gallery of continuum images for the 48 final target fields, demonstrating the range of complexity in the source structure, is included in the Appendix (Figure Set 12). Overall, we extracted 57 H I spectra from the 48 targets, including the spectra extracted from multiple continuum peaks (denoted by *A*, *B*, *C* lettering). Figure 1 displays an all-Northern-sky map of H I column density from EBHIS, with the 57 final 21-SPONGE LOS coordinates overlaid. Table 1 displays detailed source information, including coordinates, NVSS flux density (Condon et al. 1998), and rms noise in optical depth (σ_τ) computed from offline channels (0.42 km s^{-1} channel spacing). We include source information for the overly resolved and saturated sources at the bottom of Table 1.

In comparison with Table 2 of M15, we have improved σ_τ for many sources by including additional integration time and/or reprocessing the original files. Generally, $\sigma_\tau < 1 \times 10^{-3}$ (median value $= 9 \times 10^{-4}$), which makes 21-SPONGE among the highest sensitivity surveys for H I absorption ever undertaken and covers more sources than previous high-sensitivity surveys by almost a factor of 2 (e.g., Roy et al. 2013a). The outliers are due to degraded sensitivity from lack of flux density in the cases of our nine resolved sources. Overall, exceptional sensitivity to optical depth makes 21-SPONGE sensitive to absorption by H I in all stable and thermally unstable ISM phases according to predictions from steady-state ISM models.

[8] http://www.aips.nrao.edu/

[9] VLA project codes: 10C-196, 12A-256, 13A-205.

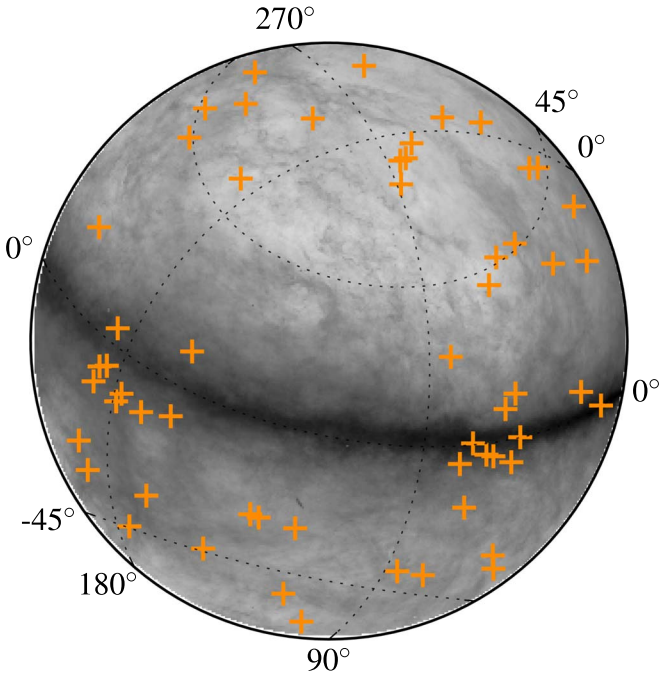

Figure 1. All-Northern-sky N(H I) map from EBHIS in zenith-equal-area projection (Winkel et al. 2016), with coordinates for the 57 21-SPONGE LOS overlaid (orange pluses). Grid lines denote Galactic coordinates.

In M15, we demonstrated excellent agreement between 21-SPONGE and other H I absorption studies by comparing the integrated H I optical depths for sources that overlap with the Millennium Arecibo H I Absorption Line Survey (Heiles & Troland 2003a, hereafter HT03), Stanimirović & Heiles (2005), and Roy et al. (2013a). Of our 48 targets, we overlap with 22/78 from HT03, 9/35 from Roy et al. (2013a), and 9/104 from Mohan et al. (2004). In Table 1 of M15, we summarized these and other external surveys. We find consistent agreement with these studies at the level of our uncertainties.

All 21-SPONGE VLA spectra will be made publicly available and are accessible via their permanent Digital Object Identifier (DOI) at this link: 10.7910/DVN/BWFKL6.

2.2. Matching H I Emission Spectra

To estimate the temperatures and column densities of H I structures using radiative transfer calculations, we need information about the brightness temperature of H I probed by our VLA absorption spectra. Observing H I emission on the same angular scale as the H I absorption measurement is ideal; however, these measurements are prohibitively expensive to conduct at an interferometric facility such as the VLA. Therefore, we obtain the expected H I brightness temperature spectra ($T_{B,\exp}(v)$) along the same LOS as the VLA targets by interpolating emission spectra from neighboring LOSs across the target position, following the strategy outlined by HT03. We obtain 21 cm emission data from the 305 m Arecibo Observatory, whose ∼4′ beam at 1.4 GHz allows us to minimize the effects of mismatched beam sizes on interpreting H I spectra. A total of 31 sources were observed as part of project A2770 at Arecibo, and 11 sources were obtained from publicly available data from HT03. Emission spectra for the remaining five sources, which lie outside of the Arecibo field of view, were obtained from the next highest resolution survey

Table 1
VLA Observation Information

Source (name)	R.A. (J2000) (hh:mm:ss)	Decl. (J2000) (dd:mm:ss)	l (°)	b (°)	$S_{1.4\,\mathrm{GHz}}$ (Jy)	Synthesized Beam ($'' \times ''$)	σ_τ ($\times 10^{-3}$)	τ_{peak}	$\int \tau\, dv$ (km s^{-1})
J0022	00:22:25.4	+00:14:56.2	107.462	−61.748	3.01	2.2 × 1.4	0.8	0.025 ± 0.001	0.148 ± 0.003
3C 018A	00:40:50.7	+10:03:05.0	118.623	−52.732	4.60	15.5 × 13.7	1.5	0.623 ± 0.004	2.404 ± 0.006
3C 018B	00:40:49.5	+10:03:50.0	118.616	−52.719	4.60	15.5 × 13.7	2.4	0.642 ± 0.006	2.305 ± 0.010
3C 041A	01:26:44.8	+33:13:02.3	131.379	−29.075	3.71	1.7 × 1.4	2.4	0.039 ± 0.004	0.343 ± 0.009
3C 041B	01:26:43.8	+33:13:21.8	131.374	−29.070	3.71	1.7 × 1.4	3.8	0.057 ± 0.006	0.317 ± 0.014
3C 48	01:37:41.3	+33:09:35.1	133.963	−28.719	16.02	1.3 × 1.2	0.7	0.050 ± 0.001	0.379 ± 0.003
4C 15.05	02:04:50.4	+15:14:11.0	147.930	−44.043	4.07	3.3 × 3.0	0.6	0.086 ± 0.001	0.723 ± 0.003
3C 78	03:08:26.2	+04:06:39.0	174.858	−44.514	5.75	4.1 × 2.2	2.2	1.366 ± 0.006	4.992 ± 0.009
4C 16.09	03:18:57.8	+16:28:32.7	166.636	−33.596	8.03	1.4 × 1.2	0.6	0.539 ± 0.002	3.019 ± 0.003
3C 111A	04:18:21.3	+38:01:35.8	161.676	−8.820	7.73	13.0 × 5.3	1.7	0.888 ± 0.005	10.167 ± 0.010
3C 111B	04:18:30.4	+38:02:30.4	161.686	−8.788	4.31	13.0 × 5.3	1.6	1.150 ± 0.005	10.225 ± 0.009
3C 111C	04:18:15.5	+38:00:48.2	161.671	−8.843	2.92	13.0 × 5.3	3.0	1.125 ± 0.009	11.367 ± 0.016
3C 120	04:33:11.1	+05:21:15.6	190.373	−27.397	3.44	4.7 × 4.3	0.9	2.033 ± 0.003	10.625 ± 0.004
3C 123A	04:37:04.9	+29:40:10.2	170.584	−11.660	49.73	20.3 × 5.3	0.6	1.750 ± 0.002	9.034 ± 0.003
3C 123B	04:37:04.0	+29:40:28.2	170.578	−11.659	49.73	20.3 × 5.3	0.7	1.783 ± 0.002	8.795 ± 0.004
3C 132	04:56:43.5	+22:49:16.3	178.862	−12.522	3.43	1.8 × 1.5	1.1	1.614 ± 0.005	7.371 ± 0.007
3C 133	05:02:58.1	+25:16:26.6	177.725	−9.913	5.77	1.2 × 1.1	2.7	1.645 ± 0.009	8.996 ± 0.015
3C 138	05:21:010.0	+16:38:22.1	187.405	−11.343	8.60	14.5 × 5.1	1.0	1.115 ± 0.003	5.949 ± 0.005
PKS 0531	05:34:44.5	+19:27:21.4	186.762	−7.108	7.02	1.3 × 1.1	0.5	0.535 ± 0.002	3.313 ± 0.003
3C 147	05:42:36.1	+49:51:07.2	161.686	10.298	22.88	4.4 × 3.8	0.5	0.796 ± 0.001	5.004 ± 0.002
3C 154	06:13:49.0	+26:04:36.7	185.592	4.003	5.00	13.7 × 12.8	0.7	1.704 ± 0.004	14.759 ± 0.006
PKS 0742	07:45:33.1	+10:11:12.7	209.797	16.592	3.51	1.9 × 1.4	0.6	0.011 ± 0.001	0.028 ± 0.003
3C 225A	09:42:15.3	+13:45:51.3	220.010	44.008	3.34	4.5 × 1.6	1.2	0.828 ± 0.002	1.487 ± 0.005
3C 225B	09:42:15.6	+13:45:49.3	220.011	44.009	3.34	4.5 × 1.6	2.3	0.791 ± 0.004	1.434 ± 0.009
3C 236	10:06:01.8	+34:54:10.4	190.065	53.980	3.24	4.8 × 1.8	0.6	0.003 ± 0.001	0.001 ± 0.003
3C 237	10:08:00.0	+07:30:16.6	232.117	46.627	6.52	6.5 × 4.4	1.0	0.410 ± 0.001	0.624 ± 0.004
3C 245A	10:42:44.6	+12:03:31.3	233.124	56.300	3.31	1.6 × 1.4	1.3	0.016 ± 0.002	0.051 ± 0.005
3C 245B	10:42:44.3	+12:03:31.6	233.123	56.299	3.31	1.6 × 1.4	4.2	0.024 ± 0.006	0.028 ± 0.015
1055+018	10:58:29.6	+01:33:58.8	251.511	52.774	3.22	0.1 × 0.0	0.9	0.008 ± 0.001	0.034 ± 0.004
3C 263.1	11:43:25.1	+22:06:56.1	227.201	73.766	3.13	7.5 × 4.4	0.7	0.020 ± 0.001	0.056 ± 0.004
3C 273	12:29:06.1	+02:03:08.6	289.945	64.359	54.99	7.8 × 4.2	0.4	0.026 ± 0.001	0.086 ± 0.002
4C 32.44	13:26:16.5	+31:54:09.5	67.234	81.048	4.86	2.8 × 1.2	0.7	0.020 ± 0.001	0.062 ± 0.003
4C 25.43	13:30:37.7	+25:09:11.0	22.468	80.988	7.05	2.8 × 1.2	1.1	0.004 ± 0.001	0.029 ± 0.004
3C 286	13:31:08.3	+30:30:33.0	56.524	80.675	14.90	5.2 × 3.3	0.4	0.007 ± 0.001	0.065 ± 0.002
4C 12.50	13:47:33.4	+12:17:24.2	347.223	70.172	5.40	4.3 × 1.5	0.9	0.091 ± 0.002	0.288 ± 0.004
3C 298	14:19:08.2	+06:28:34.8	352.160	60.666	6.10	2.4 × 1.4	0.6	0.020 ± 0.001	0.077 ± 0.003
UGC 09799	15:16:44.5	+07:01:17.8	9.417	50.120	5.50	1.7 × 1.3	6.9	0.066 ± 0.010	0.135 ± 0.024
4C 04.51	15:21:14.4	+04:30:22.0	7.292	47.747	3.93	9.4 × 3.8	0.8	0.068 ± 0.001	0.325 ± 0.003
3C 327.1A	16:04:44.9	+01:17:52.8	12.181	37.006	4.08	3.5 × 2.4	3.2	0.505 ± 0.008	2.259 ± 0.013
3C 327.1B	16:04:45.6	+01:17:47.6	12.182	37.003	4.08	3.5 × 2.4	3.0	0.448 ± 0.007	2.135 ± 0.012
PKS 1607	16:09:13.3	+26:41:29.0	44.171	46.203	4.91	0.9 × 0.4	0.6	0.177 ± 0.001	0.924 ± 0.003
J1613	16:13:41.1	+34:12:47.9	55.151	46.379	4.02	4.1 × 3.5	1.0	0.005 ± 0.001	0.001 ± 0.004
3C 345	16:42:58.8	+39:48:37.0	63.455	40.949	7.10	3.4 × 1.5	0.9	0.008 ± 0.001	0.007 ± 0.004
3C 346	16:43:48.6	+17:15:49.3	35.332	35.769	3.66	1.0 × 0.7	2.0	0.288 ± 0.004	1.160 ± 0.008
3C 390	18:45:37.6	+09:53:45.0	41.112	5.773	4.51	3.4 × 2.8	1.2	0.157 ± 0.003	2.649 ± 0.007
4C 33.48	19:24:17.5	+33:29:29.7	66.389	8.371	3.77	4.8 × 1.7	2.9	0.408 ± 0.006	2.434 ± 0.013
3C 409A	20:14:27.5	+23:34:55.4	63.398	−6.121	13.68	1.6 × 1.4	1.4	1.190 ± 0.005	8.701 ± 0.008
3C 409B	20:14:27.7	+23:34:50.2	63.398	−6.122	13.68	1.6 × 1.4	1.3	1.303 ± 0.004	8.502 ± 0.007
3C 410A	20:20:06.6	+29:42:14.8	69.212	−3.769	2.88	3.2 × 1.7	1.4	3.501 ± 0.007	17.744 ± 0.010
3C 410B	20:20:06.7	+29:42:09.6	69.211	−3.770	6.39	3.2 × 1.7	2.0	3.146 ± 0.009	16.993 ± 0.014
B2050	20:52:52.1	+36:35:35.3	78.858	−5.124	5.14	4.3 × 2.0	0.8	0.331 ± 0.002	2.653 ± 0.004
3C 433	21:23:44.6	+25:04:02.2	74.475	−17.697	10.33	9.7 × 5.7	3.0	0.467 ± 0.007	1.882 ± 0.012
PKS 2127	21:30:32.9	+05:02:17.5	58.652	−31.815	4.10	4.0 × 1.7	0.7	0.128 ± 0.001	0.556 ± 0.003
J2136	21:36:38.6	+00:41:54.2	55.473	−35.578	3.47	8.3 × 5.0	1.2	0.143 ± 0.002	0.882 ± 0.005
J2232	22:32:36.4	+11:43:50.9	77.438	−38.582	7.20	5.2 × 4.3	1.0	0.156 ± 0.002	1.052 ± 0.004
3C 454.3	22:53:58.0	+16:08:52.4	86.112	−38.185	12.66	2.2 × 1.5	1.1	0.317 ± 0.002	1.810 ± 0.005
3C 459	23:16:35.2	+04:05:18.1	83.040	−51.285	4.68	5.7 × 4.5	0.9	0.142 ± 0.002	1.146 ± 0.004
Sources rejected following preliminary observations as overly resolved (res) or saturated (sat)									
J0407 (res)	04:07:25.5	+03:40:47.3	187.651	−33.604	3.27	…	…	…	…
J0534 (res)	05:34:34.9	+22:02:07.2	184.591	−5.759	13.81	…	…	…	…
J1651 (res)	16:51:03.9	+04:59:41.9	23.039	28.967	11.2	…	…	…	…
PKS 1944 (sat)	19:46:47.9	+25:12:45.0	61.472	0.096	4.9	…	…	…	…
J2021 (sat)	20:21:38.7	+37:31:10.1	75.833	0.402	6.6	…	…	…	…

Note. Col. (1): source name. Cols. (2) through (5): R.A. and decl., l and b coordinates. Col. (6): flux density at 1.4 GHz (Condon et al. 1998). Col (7): synthesized beam size. Col. (8): rms uncertainty in optical depth, measured in offline channels (0.42 km s^{-1} channel spacing). Col. (9): peak optical depth. Col. (10): integrated optical depth, computed for channels above $3\sigma_\tau(v)$ (see Section 2.3).

available: EBHIS (10.′8 resolution at 21 cm; Winkel et al. 2016).

In Section 2.4 of M15, we described our treatment of $T_{B,\mathrm{exp}}(v)$ spectra from Arecibo. For this work, to estimate the beam efficiency factor for converting antenna temperature to brightness temperature, we compared the integrated antenna temperatures to those derived from averaging brightness temperature spectra from the Galactic Arecibo L-band Feed Array (GALFA-H I; Peek et al. 2011, 2018) survey, which is flux-calibrated based on LAB, in annuli of radius 2 pixels (16 pixels) around each target pixel. From this comparison, we derived a new beam efficiency correction factor, equal to 0.94, which we applied to the full data set and which ensures that our $T_{B,\mathrm{exp}}(v)$ spectra are consistent with previous surveys (i.e., LAB, EBHIS).

Furthermore, we note that the Arecibo H I emission spectra in this work have not been corrected for radiation entering the main telescope beam from higher order side lobes, an effect known as "stray radiation." Unlike single-dish radio telescopes whose beam shapes can be accurately modeled to remove this effect (e.g., Dwingeloo, Effelsberg, Parkes; Hartmann & Burton 1997; Kalberla et al. 2005; McClure-Griffiths et al. 2009; Kalberla & Haud 2015), Arecibo has a very complex beam structure that varies with azimuth and elevation, and therefore stray radiation is extremely difficult to remove. Comparing 21 cm emission from the GALFA-H I survey with the stray-corrected LAB survey, stray radiation likely contributes $\sim$500 mK over $\sim$50 km s^{-1} to the observed H I brightness temperature (Peek et al. 2011). Considering this effect, we are explicitly careful to not overfit our 21 cm profiles from Arecibo and emphasize that stray radiation does not affect 21 cm absorption from the VLA.

2.3. Uncertainty Arrays

The uncertainty in each spectral channel depends on the system temperature, which can be significantly increased by strong brightness temperature at Galactic velocities. To determine the frequency-dependent uncertainty arrays for each LOS, we follow the methods described in Section 3.2 of M15, which were derived following Roy et al. (2013a). In summary, for each LOS, the uncertainty array in absorption is a combination of on-source noise ($\sigma_{\mathrm{on}}(v)$) and off-source noise from the frequency-switched bandpass solution (σ_{BP}). The on-source noise is computed by scaling the rms uncertainty in $\exp{-\tau}(v)$ (i.e., our measured absorption quantity) by $(T_{B,\mathrm{LAB}}(v) + T_{\mathrm{sys,VLA}})/T_{\mathrm{sys,VLA}}$, where $T_{B,\mathrm{LAB}}(v)$ is the brightness temperature computed from adjacent pixels to each target source from the LAB survey, whose telescope at Dwingeloo is of similar size to a VLA antenna, with an assumed system temperature at the VLA of $T_{\mathrm{sys,VLA}} = 25$ K. The uncertainty in $\exp{-\tau}(v)$ is then computed by solving $\sigma_{\exp{-\tau}}(v)^2 = \sigma_{\mathrm{on}}(v)^2 + \sigma_{\mathrm{BP}}^2$. From this, we solve for the uncertainty in $\tau(v)$ (i.e., $\sigma_{\tau}(v)$) for subsequent spectral analysis. For each emission spectrum, the uncertainty array ($\sigma_{T_B}(v)$) is estimated by scaling the rms noise in $T_{B,\mathrm{exp}}(v)$ computed from offline channels by $(T_{B,\mathrm{exp}}(v) + T_{\mathrm{sys,em}})/T_{\mathrm{sys,em}}$ for an assumed system temperature of $T_{\mathrm{sys,em}} = 30$ K.

2.4. Line-of-sight Properties

In Table 1, we list parameters of the 21-SPONGE VLA spectra. First, we include the peak optical depth (τ_{peak}) along the LOS, with uncertainty equal to the value of the $\sigma_{\tau}(v)$ at the velocity of τ_{peak}. We find a median $\tau_{\mathrm{peak}} = 0.32$ and mean $\tau_{\mathrm{peak}} = 0.61$. We observe $\tau_{\mathrm{peak}} \geqslant 3$ in only two cases (3C 410A and 3C 410B). Our sources lie generally at high Galactic latitude to avoid the strong velocity crowding associated with the Galactic plane, and therefore the generally small τ_{peak} is consistent with expectations. However, we note that 13/57 LOSs lie at low Galactic latitude ($|b| < 10$), providing a comparison sample for the high-latitude population. We also list the integrated optical depth ($\int \tau\, dv$), with uncertainties computed by adding the uncertainty in each spectral channel in quadrature.

2.5. Synthetic H I Spectra

To consider the performance of our analysis methods, we will compare the 21-SPONGE spectral line pairs with a sample of synthetic 21 cm spectral line pairs from KOK14. These synthetic spectra were constructed from the 3D hydrodynamical simulation of KOK13, which includes time-varying heating and cooling of interstellar gas, momentum feedback from supernovae, self-gravity, differential rotation, and external gravity from dark matter and stars. From this simulation, KOK14 selected 10^4 randomly distributed mock sight lines at $|b| > 4.^{\circ}9$ within the simulated volume and extracted the number density (n), temperature (kinetic, T_k, and spin, T_s), and velocity (v) as a function of distance along the LOS. Using analytic radiative transfer and simple line excitation considerations, KOK14 constructed synthetic 21 cm brightness temperature (T_B) and optical depth (τ) spectra from each LOS. We refer the reader to Section 2.3 of KOK14 for details of synthetic spectra construction.

In Murray et al. (2017), we found that the implementation of the WF effect has a significant effect on the line widths of the KOK14 synthetic spectral lines and the resulting WNM spin temperature distribution. KOK14 constructed three sets of synthetic 21 cm data for different WF prescriptions: no WF, constant WF, and maximum WF (i.e., $T_s = T_k$). We found that the constant WF case, wherein the Lyα radiation field density was fixed at 10^{-6} photons cm^{-3}, resulted in a narrow spin temperature distribution ($T_s \sim 4000$ K for $T_k > 4000$ K) for the WNM (cf. Figure 2 of KOK14). Via comparison with 21-SPONGE spectra, we found that KOK14 spectra—whether with no WF or with constant WF—feature a significant population of large-amplitude, wide absorption components not observed in 21-SPONGE yet well above our sensitivity limits (cf. Figure 11 of Murray et al. 2017). Furthermore, these components correspond to WNM properties not observed by 21-SPONGE (i.e., $T_s \sim$ 3000–4000 K). From this comparison, we concluded that a more sophisticated treatment of the WF effect is likely necessary to produce realistic synthetic spectral lines from future simulations.

For this study, we select the maximum WF synthetic data set from KOK14. Using an analysis similar to that of Murray et al. (2017), we determined that the maximum WF dataset features spectral components whose line widths agree best with those detected in 21-SPONGE and therefore maximizes consistency between observed and synthetic data sets. To build the synthetic data set, we select spectra without saturated ($\tau \geqslant 3$)

absorption, for a final catalog of 9355 H I spectral pairs. To simulate the same observational properties of 21-SPONGE spectral line pairs, we add Gaussian noise to each synthetic 21 cm spectrum (rms $\sigma_\tau = 10^{-3}$ for absorption, rms $\sigma_{T_B} = 0.2$ K for emission) as done in Murray et al. (2017).

3. Analysis

To derive the physical properties of individual H I structures along each LOS, we decompose all H I emission and absorption spectral line pairs into Gaussian functions. In the following section, we describe our method for autonomously decomposing 21 cm spectra.

3.1. Gaussian Decomposition

We begin by decomposing the VLA H I absorption spectra uniformly using the Autonomous Gaussian Decomposition algorithm (AGD; Lindner et al. 2015) via its open-source Python implementation, GaussPy.[10] AGD implements derivative spectroscopy and supervised machine learning to produce efficient, reproducible guesses for the basic parameters of Gaussian functions, including the number of components, their amplitudes, positions, and widths. Following the method described in Lindner et al. (2015) and employed in Murray et al. (2017), we train the algorithm using a synthetic absorption-line data set constructed from spectral line parameters from HT03. From the training process, we determine optimal values of the two-phase smoothing parameters, $\alpha_1 = 1.12$ and $\alpha_2 = 2.75$, required by AGD to compute spectral line parameter guesses. We then decompose the 21-SPONGE absorption lines using these values with an imposed minimum signal-to-noise ratio of $S/N = 3$. To avoid aliasing narrow components, we first resample the spectra to a velocity resolution of 0.1 km s^{-1} (Lindner et al. 2015). As shown in Lindner et al. (2015) and Murray et al. (2017), the resulting parameters of the decomposition are statistically indistinguishable from those found in the by-hand analysis of 21-SPONGE sources. Although no Gaussian decomposition represents a unique solution, we emphasize the benefits of the AGD: to eliminate subjective biases of human-derived guesses and to ensure that the decomposition results are completely reproducible.

After decomposing each H I absorption spectrum using AGD into N components, we produce a model for the optical depth along the LOS:

$$\tau(v)_{\rm AGD} = \sum_{n=0}^{N-1} \tau_{0,n} \cdot e^{-4\ln 2(v-v_{0,n})^2/\Delta v_n^2}, \quad (1)$$

where ($\tau_{0,n}$, $v_{0,n}$, Δv_n) are the amplitude, mean velocity, and FWHM of the nth component.

To fit these components to the expected brightness temperature along the LOS ($T_{B,\rm exp}(v)$), we assume a two-component H I medium, wherein some clouds contribute both opacity and brightness temperature (i.e., detected in emission and absorption), and some clouds are dominated by the WNM and contribute only brightness temperature to the LOS (e.g., Mebold et al. 1997; Dickey et al. 2000, HT03, M15). For each LOS, we solve,

$$T_{B,\rm exp,AGD}(v) = T_{B,\rm abs,AGD}(v) + T_{B,\rm em,AGD}(v). \quad (2)$$

To determine the contributions of absorption-detected and emission-only components to $T_{B,\rm exp}(v)$, we implement a new method to fit all components to $T_{B,\rm exp}(v)$ using AGD, based on the strategy described in HT03. We note that whereas the original HT03 method involved fitting components by eye, our new method is autonomous. The method involves the following steps:

1. Fit all N components from $\tau(v)$ to $T_{B,\rm exp}(v)$ via a least-squares fit. The mean velocities and widths are allowed to vary by $\pm 10\%$ to simulate small random fluctuations and their amplitudes are constrained so that $0 < T_{B,n} = T_{s,n} \cdot (1 - e^{-\tau_{0,n}})$ and $T_{s,n} \leqslant T_{k,\max,n} = 21.866 \cdot \Delta v_n^2$ to produce realistic spin temperatures.
2. Subtract the best-fit model in step (1) from $T_{B,\rm exp}(v)$ to produce a residual emission spectrum, which contains only emission not detected in absorption.
3. Apply GaussPy to fit K new components to the residual emission spectrum from (2), using the trained one-phase value of $\alpha = 3.75$ and $S/N \geqslant 5$ from previous analysis of HT03 emission spectra (Murray et al. 2017). The S/N requirement is stricter in the fit to emission than the initial absorption fit so that we avoid overfitting the emission residuals in the presence of stray radiation. We also remove any component guesses whose mean velocities agree with previously detected absorption components within 1 spectral channel (i.e., 0.42 km s^{-1}) so as not to spuriously overfit $T_{B,\rm exp}(v)$ (this occurs only in the presence of strong residuals following the subtraction of absorption components in complex LOS).
4. Combine the $N + K$ Gaussian components from steps (1) and (3) and execute a final least-squares fit to $T_{B,\rm exp}(v)$. In this final fit, we allow all mean velocities and widths to vary by 10%, and constrain all amplitudes such that $T_{B,\rm exp} > 0$. In this step, initial estimates of T_s for the N absorption components and the Gaussian parameters of the K emission-only components are computed.

Given a final list of $N + K$ Gaussian components fitted to $T_{B,\rm exp}(v)$ from the procedure described above, we solve Equation (2) for all possible orderings of the N absorption components along the LOS and for varying absorption properties of the K emission-only components, following HT03. In detail, we solve:

$$T_{B,\rm abs,AGD}(v) = \sum_{n=0}^{N-1} T_{s,n}(1 - e^{-\tau_n(v)}) e^{-\sum_{m=0}^{M} \tau_m(v)}, \quad (3)$$

where the subscript m refers to all components which lie in front of the nth component, and

$$T_{B,\rm em,AGD}(v) = \sum_{k=0}^{K-1} [\mathscr{F}_k + (1 - \mathscr{F}_k)\, e^{-\tau(v)}] \cdot T_{0,k}\, e^{\frac{-4\ln 2(v-v_{0,k})^2}{\Delta v_k^2}}, \quad (4)$$

where ($T_{0,k}$, $v_{0,k}$, Δv_k) are the amplitude, mean velocity, and FWHM of the kth component fitted only in emission, and $\mathscr{F}_k$ is the fraction of each component lying in front of all absorption components. Previous analysis has shown that $\mathscr{F}$ is highly

[10] GaussPy; https://github.com/gausspy/gausspy.

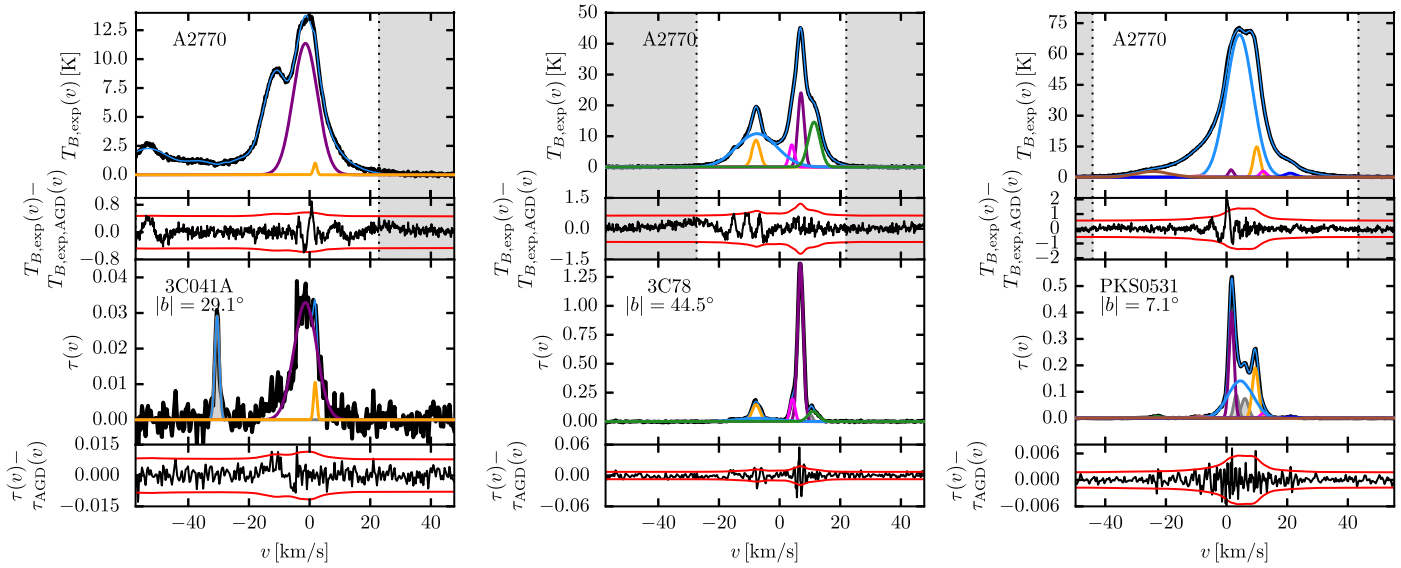

Figure 2. Examples displaying the Gaussian fits to 21-SPONGE H I emission and absorption spectral line pairs described in Section 3. In each panel, we plot the emission ($T_{B,\rm exp}(v)$; top) and absorption ($\tau(v)$; bottom) spectra. The residual spectra following the Gaussian fits are included below each panel, with $\pm 3 \times \sigma_\tau(v)$ and $\sigma_{TB}(v)$, respectively (red). We plot all fitted absorption components in the bottom panel. Components whose derived spin temperatures are unphysical (i.e., $\leqslant$10 K) are plotted in gray, and components with $T_s > 10$ K are plotted in matching colors in the middle and top panels. The total fits, $T_{B,\rm exp,AGD}(v)$ and $\tau_{\rm AGD}(v)$, are displayed in thin blue lines. The source of $T_{B,\rm exp}(v)$, whether from Arecibo (A2770 or HT03) or EBHIS, is printed in the top panels. In the bottom panels, we print the source name and the absolute Galactic latitude ($|b|$). Finally, in the top panels, we shade in gray the velocities where $T_{B,\rm exp}(v) \leqslant 3 \cdot \sigma_{T_B}(v)$ to illustrate the range over which LOS column densities are computed (i.e., the unshaded region is used). If no vertical shading is present, the full displayed velocity range is used. Plots for all sources are included in the Appendix.

uncertain (e.g., HT03; Stanimirović et al. 2014; M15) and yet it has a significant effect on the derived spin temperatures. Therefore, following HT03, we allow $\mathscr{F}_k$ to have one of three values, $\mathscr{F}_k = 0.0$, 0.5, or 1.0 for all K emission-only components.

Furthermore, the order of the absorption components along the LOS will only affect $T_{B,\rm abs}(v)$ in the cases of components that overlap significantly in velocity (HT03). For each LOS, there are a maximum of $N!$ possible orderings, but we select only the unique orderings corresponding to components that overlap in area by more than $3\sigma_\tau dv$. Therefore, there are a total of $3 \times N!$ possible iterations for the final fit to Equation (2), but in practice there are many fewer for each LOS.

We determine a final estimate for the spin temperature of each absorption-detected component by computing the weighted mean and standard deviation over all ordering trials (cf. Equations (21a) and (21b) of HT03). We fit a total of 280 absorption components and 278 emission-only components to the 57 LOSs. Figure 2 displays three examples of the fitting process described above. Similar plots for all 57 LOSs are included in the Appendix, Figure Set 13.

3.2. Synthetic H I Decomposition

We use the same methodology described above to fit 9355 synthetic H I absorption and emission spectral line pairs from KOK14 with maximum WF. In contrast to the analysis of Murray et al. (2017), wherein we presented a method for matching Gaussian spectral lines to "true" gas structures along the LOS, the new method presented here improves the statistics of components for which we can derive T_s and $N(\rm H\,I)$. The method described in Murray et al. (2017) selected only those components with unambiguous signatures in $\tau(v)$, $T_{B,\rm exp}(v)$, and n/T_s, and therefore resulted in fewer detected components per LOS. Here we fit a total of 12,715 components to the 9355 synthetic absorption lines.

4. Fitting Results

4.1. Properties of Fitted Components

For each absorption-detected component, we compute the maximum kinetic temperature ($T_{k,\rm max}$) via

$$T_{k,\rm max} = \frac{m_{\rm H}}{8 k_{\rm B} \ln 2} \Delta v_0^2 = 21.866 \cdot \Delta v_0^2 \quad (5)$$

for hydrogen mass $m_{\rm H}$ and Boltzmann's constant $k_{\rm B}$ (Draine 2011).

Next, we compute the H I column density per absorption component, given by

$$N(\rm H\,I)_{\rm abs} = C_0 \int \tau\, T_s\, dv = 1.064 \cdot C_0 \cdot \tau_0 \cdot \Delta v_0 \cdot T_s, \quad (6)$$

where $C_0 = 1.823 \times 10^{18}\,\rm cm^{-2}/(km\,s^{-1}\,K)$, Δv_0 is measured in $\rm km\,s^{-1}$, and 1.064 converts the product to the area under a Gaussian function with the given height and width.

Figure 3 displays cumulative distribution functions (CDFs) of the fitted parameters for all absorption-detected components with physically reasonable values of T_s, defined as $T_s > 10$ K. This limit for "reasonable" temperatures is defined conservatively based on the estimated contribution of the cosmic microwave and Galactic synchrotron backgrounds at the locations of our sources, which we found to vary between 2.76 and 2.85 K for sources from the first half of the 21-SPONGE survey (M15), plus an estimated minimum T_k of the CNM ($\sim$7 K; Wolfire et al. 2003). Out of 280 components, 222 have $T_s > 10$ K.

In the top row of Figure 3, we display parameters from the best fit to $\tau(v)$, including optical depth amplitude (τ_0), FHWM (Δv_0), and absolute mean velocity ($|v_0|$). In the bottom row, we

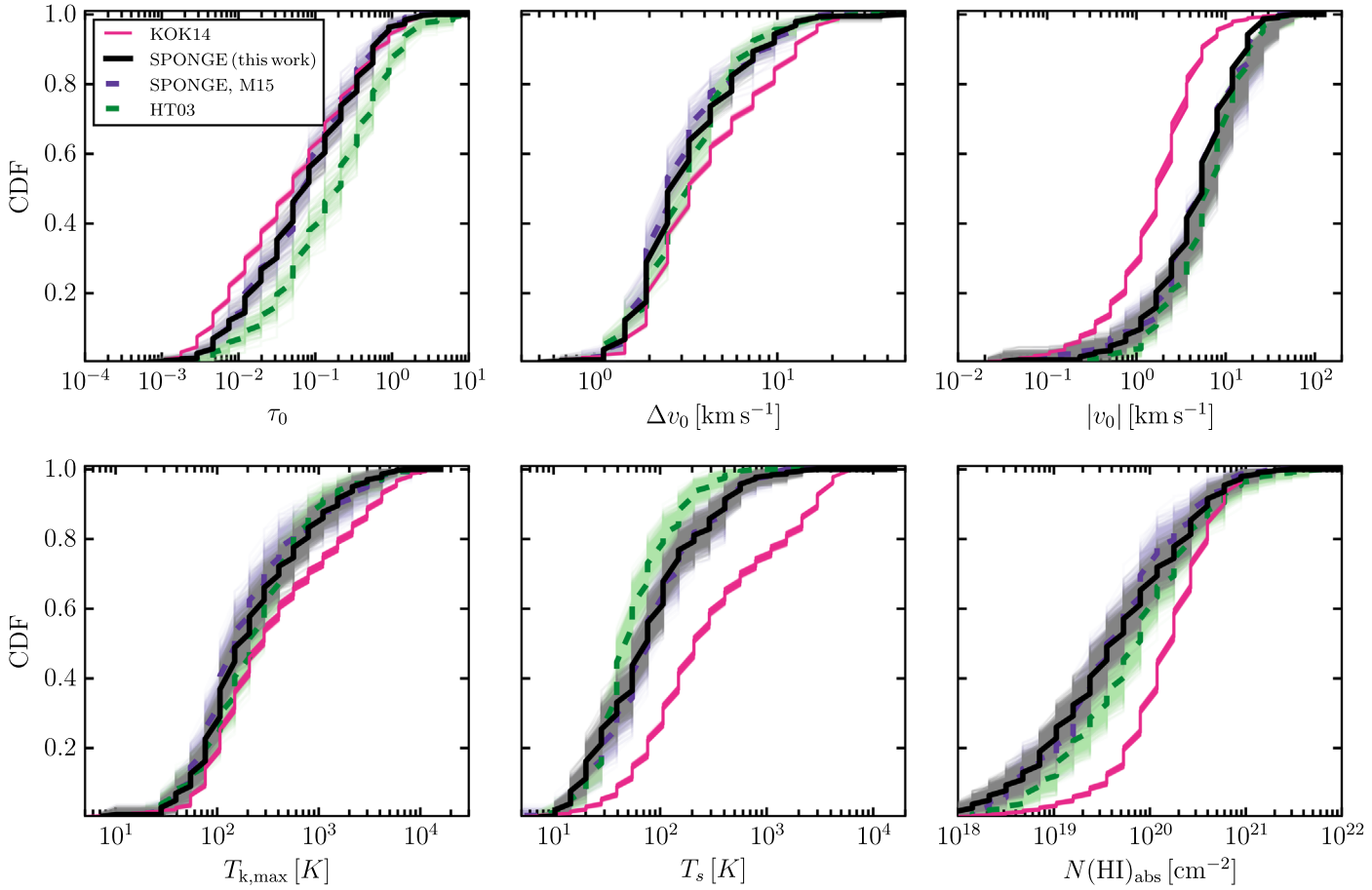

Figure 3. Parameters derived from the Gaussian fits to the 57 21-SPONGE absorption lines (280 components) via AGD (Section 3.1; black). These include optical depth amplitude (τ_0), FWHM (Δv_0) and mean velocity ($|v_0|$), maximum kinetic temperature ($T_{k,\rm max}$), spin temperature (T_s), and column density (N(H I)). For comparison, we include the results of HT03 (green dashed), the first half of the 21-SPONGE survey (M15; purple dashed), and a fit to KOK14 synthetic H I spectral line pairs using the same methodology (pink).

include derived physical properties. In all panels of Figure 3, we bootstrap each sample over 100 trials and include the resampled CDFs to illustrate the effect of outliers on the distributions. For comparison, we include the results of HT03, M15, and a reprocessing of the synthetic H I spectral line pair database from KOK14 with maximum WF (Section 3.2). The parameters for all 21-SPONGE sources are listed in Table 5 in the Appendix. The uncertainties for all parameters are computed as part of the least-squares AGD fit, except for the uncertainty in T_s (and, subsequently N(H I)$_{\rm abs}$), which is computed following the iterations over LOS component ordering. We set the minimum uncertainty in the optical depth amplitudes equal to $\sigma_\tau(v)$ at the position of each component, and the minimum uncertainty in the mean velocity and FWHM is equal to 0.1 km s^{-1}. We note that for one absorption component toward 3C 111A, the uncertainties from the AGD fit are extremely large ($\gg$1000)—this component was not recovered in the fit to $T_{B,\rm exp}(v)$, and we identify it by setting the uncertainties in its component parameters equal to 99 in Table 5.

In comparison with the previous observations shown in Figure 3, we find that our decomposition results (black) are statistically indistinguishable from the by-hand analysis of the first half of the 21-SPONGE survey (purple dashed; M15 wherein we analyzed a subset of the 21-SPONGE sample presented in this work. We are also generally consistent with HT03, except in the case of τ_0, wherein the superior sensitivity of 21-SPONGE allows us to probe smaller H I optical depths. In addition, we detect a higher T_s in the present analysis than found by HT03, which is also attributable to our improved observational sensitivity.

In Figure 3, we find that the observed (SPONGE, HT03) and synthetic (KOK14) T_s and N(H I) distributions are significantly different. We will discuss this further in Section 6.

4.2. Correspondence between 21 cm Absorption and Emission

Overall, most (78%) of the N fitted components to $\tau(v)$ have corresponding components in the fit to $T_{B,\rm exp}(v)$. Even when all $\tau(v)$ components are forced to be included in the fit to $T_{B,\rm exp}(v)$ (e.g., as in the method of HT03, M15), ∼10% of components end up with unphysical spin temperatures. Components with $T_s \leqslant 10$ K are displayed in gray in Figure Set 13.

However, the overall fraction of absorption components with corresponding detected emission is generally high: for 22% of the 57 LOSs, 100% of the absorption-fitted components correspond to components in the fit to $T_{B,\rm exp}(v)$, and for 98% of LOSs, $\geqslant$50% of absorption components correspond to $T_{B,\rm exp}(v)$ components. The LOSs featuring the lowest fraction of corresponding components between absorption and emission tend to lie at low Galactic latitude, where velocity blending of spectral lines is strongest. We find consistent statistics in the decomposition of KOK14 spectra. We will discuss the

implications of the observed correspondence between absorption and emission further in Section 6.1.

An important effect in producing absorption components with no corresponding emission components (i.e., components with $T_s < 10$ K) is beam mismatch between absorption and emission. In addition, 21 cm emission profiles are necessarily measured using adjacent LOSs from the absorption profile in order to avoid the background continuum source, which means that the two profiles are not sampling identical populations of H I structures. For emission spectra from Arecibo (e.g., A2770, HT03), $T_{B,\mathrm{exp}}(v)$ is computed on $\sim 4'$ scales, and for those from EBHIS, $T_{B,\mathrm{exp}}(v)$ is computed on $10\farcm8$ scales, in contrast with sub-arcminute scales for absorption from the VLA. An example of this effect is shown in the case of 3C 041A (Figure 2) .The absorption line clearly detected at $v \sim -30\,\mathrm{km\,s^{-1}}$ is not recovered in $T_{B,\mathrm{exp}}(v)$, likely due to a beam mismatch or LOS effect.

We find that varying the decomposition scheme described in Section 3.1 did not have a significant effect on the results or derived physical parameters. Allowing the component parameters to vary by between 1% and 20% in step (1) has the largest effect on the number and properties of the fitted emission-only components. For example, the fraction of absorption-detected components recovered in the fit to $T_{B,\mathrm{exp}}(v)$ and their derived T_s values do not vary significantly for different allowed variances.

5. Column Densities

Following decomposition, we compute and compare different estimates of the total column density along 21-SPONGE LOSs. Given that the majority of our 21 cm brightness temperatures have not been corrected for stray radiation, we conservatively restrict our analysis of $T_{B,\mathrm{exp}}(v)$ to channels above the uncertainty array for each LOS, specifically: $T_{B,\mathrm{exp}}(v) \geqslant 3\ \sigma_{T_B}(v)$. In the top panels of each source plot in Figures 2 and 13 we shade the velocity channels which are not used in the column density analysis in light gray. The minimum and maximum velocities satisfying $T_{B,\mathrm{exp}}(v) \geqslant 3\ \sigma_{T_B}(v)$ are referred to in subsequent discussion as $v_{\mathrm{em,min}}$ and $v_{\mathrm{em,max}}$, respectively.

In the absence of optical depth information, it is common in the literature to assume that neutral gas is optically thin so that the LOS column density can be computed via

$$N(\mathrm{H\,I})_{\mathrm{thin}} = C_0 \int_{v_{\mathrm{em,min}}}^{v_{\mathrm{em,max}}} T_{B,\mathrm{exp}}(v)\, dv, \tag{7}$$

where dv is measured in $\mathrm{km\,s^{-1}}$. Incorporating the optical depth information from 21-SPONGE, assuming that all H I within each velocity channel is isothermal (e.g., Dickey & Benson 1982; Chengalur et al. 2013), the column density is given by

$$N(\mathrm{H\,I})_{\mathrm{iso}} = C_0 \int_{v_{\mathrm{em,min}}}^{v_{\mathrm{em,max}}} \frac{\tau(v)\, T_{B,\mathrm{exp}}(v)}{1 - e^{-\tau(v)}}\, dv. \tag{8}$$

However, considering significant overlap in the velocity of individual spectral features in Figure Set 13, there may be multiple H I structures with different physical properties within the same radial velocity channels, potentially invalidating the isothermal approximation in Equation (8). Using the results of our spectral decomposition, we compute the "total" H I column density,

$$N(\mathrm{H\,I})_{\mathrm{total}} = \sum_{n=0}^{N-1} N(\mathrm{H\,I})_{\mathrm{abs},n} + C_0 \int_{v_{\mathrm{em,min}}}^{v_{\mathrm{em,max}}} \left(\sum_{k=0}^{K-1} T_{0,k} e^{\frac{-4\ln 2 (v - v_{0,k})^2}{\Delta v_k^2}} \right) dv, \tag{9}$$

where we first sum over the column densities of all N components detected in both absorption and emission ($N(\mathrm{H\,I})_{\mathrm{abs}}$; Equation (6)) and then add the total brightness temperature of the K components detected in emission only for channels above $3\sigma_{T_B}(v)$ (i.e., between $v_{\mathrm{em,min}}$ and $v_{\mathrm{em,max}}$) under the optically thin approximation. We restrict the integration of the emission-only components so that $N(\mathrm{H\,I})_{\mathrm{total}}$ can be compared with $N(\mathrm{H\,I})_{\mathrm{thin}}$ and $N(\mathrm{H\,I})_{\mathrm{iso}}$. The uncertainty in $N(\mathrm{H\,I})_{\mathrm{total}}$ is computed as the standard deviation over 1000 Monte Carlo trials for each LOS wherein all Gaussian component parameters are drawn from a normal distribution around each parameter (e.g., Heiles & Troland 2003b; Stanimirović et al. 2014).

In Table 2, we list $N(\mathrm{H\,I})_{\mathrm{thin}}$, $N(\mathrm{H\,I})_{\mathrm{iso}}$, and $N(\mathrm{H\,I})_{\mathrm{total}}$ for all 57 21-SPONGE LOSs, with uncertainties propagated in quadrature from $\sigma_{T_B}(v)$, $\sigma_\tau(v)$ for $N(\mathrm{H\,I})_{\mathrm{thin}}$ and $N(\mathrm{H\,I})_{\mathrm{iso}}$. We observe that $N(\mathrm{H\,I})_{\mathrm{total}}$ and $N(\mathrm{H\,I})_{\mathrm{iso}}$ are consistent within uncertainties, indicating that our autonomous decomposition method is performing well and recovering the majority of $\tau(v)$ for all LOSs.

To compare these column densities, we explore the effect of optical depth on the LOS column density by estimating the "correction factor" to be applied to $N(\mathrm{H\,I})_{\mathrm{thin}}$ to account for optical depth effects. Specifically, we compute two versions, one for the isothermal column density, $\mathcal{R}_{\mathrm{iso}} = N(\mathrm{H\,I})_{\mathrm{iso}}/N(\mathrm{H\,I})_{\mathrm{thin}}$, and one for the "total" column density, $\mathcal{R}_{\mathrm{total}} = N(\mathrm{H\,I})_{\mathrm{total}}/N(\mathrm{H\,I})_{\mathrm{thin}}$. In Figure 4, we plot $\mathcal{R}_{\mathrm{iso}}$ and $\mathcal{R}_{\mathrm{total}}$ as a function of $N(\mathrm{H\,I})_{\mathrm{thin}}$. For low H I column densities, $N(\mathrm{H\,I})_{\mathrm{thin}} \lesssim 5 \times 10^{20}\,\mathrm{cm^{-2}}$, $\mathcal{R}_{\mathrm{iso}}$ and $\mathcal{R}_{\mathrm{total}}$ are equal to or consistent with unity within uncertainties. The scatter is larger (and uncertainties are higher) in the case of $\mathcal{R}_{\mathrm{total}}$ due to the uncertainty in fitting components between absorption and emission. In particular, the uncertainty in $\mathcal{R}_{\mathrm{total}}$ is only significant at low Galactic latitudes where significant line blending yields large uncertainties in fitted parameters.

In Figure 4, $\mathcal{R}_{\mathrm{iso}}$ and $\mathcal{R}_{\mathrm{total}}$ exhibit the same overall behavior as a function of $N(\mathrm{H\,I})_{\mathrm{thin}}$, which has also been pointed out and discussed as part of a recent study of H I in the Perseus molecular cloud (Lee et al. 2015) and recent analysis of data from HT03 and the first half of the 21-SPONGE survey (Nguyen et al. 2018). This agreement indicates that our autonomous spectral decomposition method recovers well the velocity structure of 21 cm absorption and emission for the majority of sources. We will discuss this further in Section 6.1.

In Table 2, we also include the total column density along each LOS in the CNM and UNM phases, $N(\mathrm{H\,I})_{\mathrm{CNM}}$ and $N(\mathrm{H\,I})_{\mathrm{UNM}}$, as the sum of all components with $T_{s,\mathrm{CNM}} \leqslant 250$ K and $250 < T_{s,\mathrm{UNM}} \leqslant 1000$ K (defined following predictions from Wolfire et al. 2003 in the solar circle), respectively. We then estimate the fraction of $N(\mathrm{H\,I})_{\mathrm{total}}$ in each phase, with the assumption that the remaining mass is in the WNM. These mass fraction estimates are uncertain, as both uncertainties in the observations and the AGD-based fit contribute. To estimate the uncertainties in f_{CNM} and f_{UNM}, we compute the standard deviation of $N(\mathrm{H\,I})_{\mathrm{CNM}}$ and $N(\mathrm{H\,I})_{\mathrm{UNM}}$ over the Monte Carlo

Table 2
Column Densities

Source (name)	$N(\mathrm{H\,I})_{\mathrm{thin}}$ (10^{20} cm^{-2})	$N(\mathrm{H\,I})_{\mathrm{iso}}$ (10^{20} cm^{-2})	$N(\mathrm{H\,I})_{\mathrm{total}}$ (10^{20} cm^{-2})	$N(\mathrm{H\,I})_{\mathrm{CNM}}$ (10^{20} cm^{-2})	$N(\mathrm{H\,I})_{\mathrm{UNM}}$ (10^{20} cm^{-2})	f_{CNM}	f_{UNM}
J0022	2.63 ± 0.14	2.64 ± 0.14	2.63 ± 0.08	0.11	0.88	0.04 ± 0.07	0.33 ± 0.37
3C018A	5.65 ± 0.02	6.29 ± 0.03	6.71 ± 0.24	3.29	0.00	0.49 ± 0.21	0.00 ± 0.28
3C018B	5.65 ± 0.02	6.27 ± 0.03	6.67 ± 0.24	3.29	0.00	0.49 ± 0.22	0.00 ± 0.42
3C041A	5.43 ± 0.23	5.46 ± 0.23	5.46 ± 0.11	0.02	1.99	0.00 ± 0.10	0.37 ± 0.51
3C041B	5.43 ± 0.23	5.47 ± 0.23	5.47 ± 0.08	0.88	0.00	0.16 ± 0.15	0.00 ± 0.76
3C48	4.24 ± 0.26	4.27 ± 0.26	4.26 ± 0.05	0.16	1.53	0.04 ± 0.14	0.36 ± 0.21
4C15.05	4.33 ± 0.15	4.42 ± 0.16	4.42 ± 0.24	0.39	3.11	0.09 ± 0.04	0.70 ± 0.18
3C78	9.76 ± 0.22	11.44 ± 0.26	11.37 ± 0.86	4.43	3.17	0.39 ± 0.20	0.28 ± 0.24
4C16.09	9.96 ± 0.16	11.01 ± 0.17	10.93 ± 0.28	4.36	2.37	0.40 ± 0.24	0.22 ± 0.08
3C111A	24.25 ± 1.06	28.43 ± 1.24	28.60 ± 1.25	19.82	0.69	0.69 ± 0.18	0.02 ± 0.09
3C111B	24.25 ± 1.06	28.60 ± 1.24	28.04 ± 1.78	9.97	8.86	0.36 ± 0.22	0.32 ± 0.09
3C111C	24.25 ± 1.06	29.21 ± 1.27	24.14 ± 3.17	13.17	0.00	0.55 ± 0.22	0.00 ± 0.19
3C120	10.02 ± 0.03	15.85 ± 0.04	14.07 ± 1.09	7.48	0.00	0.53 ± 0.24	0.00 ± 0.08
3C123A	15.04 ± 0.71	19.62 ± 0.93	19.75 ± 3.55	5.57	5.36	0.28 ± 0.24	0.27 ± 0.10
3C123B	15.04 ± 0.71	19.51 ± 0.92	19.68 ± 3.61	5.73	6.07	0.29 ± 0.22	0.31 ± 0.19
3C132	22.83 ± 0.27	27.15 ± 0.32	24.95 ± 2.04	8.51	0.00	0.34 ± 0.14	0.00 ± 0.07
3C133	25.11 ± 0.07	30.07 ± 0.09	28.80 ± 2.13	3.01	15.93	0.10 ± 0.08	0.55 ± 0.14
3C138	18.55 ± 0.18	21.32 ± 0.20	20.82 ± 2.21	7.16	0.89	0.34 ± 0.12	0.04 ± 0.07
PKS0531	25.13 ± 0.36	27.10 ± 0.39	27.15 ± 1.74	1.61	14.65	0.06 ± 0.26	0.54 ± 0.07
3C147	17.26 ± 0.33	18.71 ± 0.35	18.43 ± 1.50	7.14	0.00	0.39 ± 0.18	0.00 ± 0.04
3C154	34.11 ± 0.05	46.48 ± 0.07	38.87 ± 10.88	2.26	26.60	0.06 ± 0.38	0.68 ± 0.32
PKS0742	3.13 ± 0.19	3.13 ± 0.20	3.11 ± 0.09	0.09	0.00	0.03 ± 0.05	0.00 ± 0.25
3C225A	3.53 ± 0.03	3.65 ± 0.03	3.63 ± 0.10	0.42	0.64	0.12 ± 0.08	0.18 ± 0.40
3C225B	3.53 ± 0.03	3.65 ± 0.03	3.65 ± 0.13	0.62	1.00	0.17 ± 0.14	0.27 ± 0.71
3C236	0.78 ± 0.15	0.78 ± 0.15	0.78 ± 0.15	0.00	0.00	0.00 ± 0.20	0.00 ± 0.99
3C237	2.16 ± 0.03	2.19 ± 0.03	2.19 ± 0.08	0.13	0.63	0.06 ± 0.11	0.29 ± 0.57
3C245A	2.19 ± 0.13	2.20 ± 0.13	2.19 ± 0.09	0.00	0.40	0.00 ± 0.15	0.18 ± 0.73
3C245B	2.19 ± 0.13	2.20 ± 0.13	1.92 ± 0.13	0.00	0.00	0.00 ± 0.45	0.00 ± 1.00
1055+018	2.94 ± 0.16	2.94 ± 0.16	2.94 ± 0.08	0.00	0.83	0.00 ± 0.07	0.28 ± 0.37
3C263.1	1.81 ± 0.18	1.81 ± 0.18	1.81 ± 0.00	0.03	0.00	0.02 ± 0.16	0.00 ± 0.82
3C273	2.11 ± 0.05	2.11 ± 0.05	2.10 ± 0.08	0.02	0.29	0.01 ± 0.05	0.14 ± 0.24
4C32.44	1.17 ± 0.14	1.17 ± 0.14	1.16 ± 0.01	0.11	0.07	0.10 ± 0.14	0.06 ± 0.69
4C25.43	1.07 ± 0.12	1.07 ± 0.12	1.04 ± 0.12	0.00	0.00	0.00 ± 0.25	0.00 ± 1.00
3C286	1.10 ± 0.15	1.10 ± 0.15	1.10 ± 0.01	0.09	0.00	0.08 ± 0.10	0.00 ± 0.48
4C12.50	2.07 ± 0.10	2.10 ± 0.11	2.09 ± 0.06	0.33	0.66	0.16 ± 0.11	0.31 ± 0.54
3C298	2.05 ± 0.11	2.06 ± 0.12	2.06 ± 0.23	0.15	0.00	0.07 ± 0.08	0.00 ± 0.38
UGC09799	2.90 ± 0.14	2.91 ± 0.14	2.91 ± 0.03	0.17	0.00	0.06 ± 0.49	0.00 ± 1.00
4C04.51	4.02 ± 0.17	4.06 ± 0.17	3.99 ± 0.04	1.13	0.00	0.28 ± 0.05	0.00 ± 0.24
3C327.1A	7.21 ± 0.17	7.87 ± 0.18	7.87 ± 0.19	3.34	0.00	0.42 ± 0.12	0.00 ± 0.47
3C327.1B	7.21 ± 0.17	7.83 ± 0.18	7.87 ± 0.21	3.26	0.00	0.41 ± 0.11	0.00 ± 0.44
PKS1607	3.78 ± 0.14	3.88 ± 0.14	3.86 ± 0.11	0.89	0.00	0.23 ± 0.09	0.00 ± 0.20
J1613	1.50 ± 0.14	1.50 ± 0.14	1.50 ± 0.14	0.00	0.00	0.00 ± 0.16	0.00 ± 0.80
3C345	0.71 ± 0.06	0.71 ± 0.06	0.71 ± 0.06	0.00	0.00	0.00 ± 0.29	0.00 ± 1.00
3C346	5.00 ± 0.15	5.19 ± 0.16	5.21 ± 0.10	1.45	0.00	0.28 ± 0.09	0.00 ± 0.44
3C390	25.05 ± 1.13	25.91 ± 1.17	26.00 ± 0.80	3.05	10.52	0.12 ± 0.02	0.40 ± 0.08
4C33.48	13.48 ± 0.39	14.04 ± 0.40	13.80 ± 0.44	1.58	0.00	0.11 ± 0.06	0.00 ± 0.27
3C409A	23.00 ± 0.80	27.74 ± 0.96	27.05 ± 2.27	12.96	0.63	0.48 ± 0.19	0.02 ± 0.08
3C409B	23.00 ± 0.80	27.66 ± 0.96	25.63 ± 1.85	7.11	7.67	0.28 ± 0.21	0.30 ± 0.08
3C410A	38.53 ± 2.81	54.10 ± 3.94	53.13 ± 7.24	24.46	0.99	0.46 ± 0.20	0.02 ± 0.14
3C410B	38.53 ± 2.81	53.31 ± 3.88	42.87 ± 18.06	16.17	0.00	0.38 ± 0.31	0.00 ± 0.08
B2050	23.59 ± 1.20	24.56 ± 1.25	24.54 ± 0.84	3.49	3.79	0.14 ± 0.11	0.15 ± 0.05
3C433	8.38 ± 0.04	8.88 ± 0.04	8.86 ± 0.29	2.11	0.00	0.24 ± 0.10	0.00 ± 0.39
PKS2127	4.62 ± 0.28	4.71 ± 0.29	4.70 ± 0.24	0.67	1.59	0.14 ± 0.04	0.34 ± 0.19
J2136	4.36 ± 0.05	4.49 ± 0.06	4.40 ± 0.20	0.68	0.00	0.16 ± 0.07	0.00 ± 0.34
J2232	4.88 ± 0.16	5.00 ± 0.16	4.98 ± 0.07	1.48	0.00	0.30 ± 0.10	0.00 ± 0.26
3C454.3	6.84 ± 0.08	7.05 ± 0.08	6.91 ± 0.56	1.97	0.00	0.28 ± 0.10	0.00 ± 0.21
3C459	5.43 ± 0.16	5.60 ± 0.16	5.56 ± 0.71	0.32	4.27	0.06 ± 0.33	0.77 ± 0.29

Note. Col. (1): source name. Col. (2): optically thin H I column density (Equation (7)). Col. (3): isothermal H I column density (Equation (8)). Col. (4): total H I column density following the autonomous computation of T_s and $N(\mathrm{H\,I})_{\mathrm{abs}}$ for individual spectral components (Equation (9)). Col. (5): sum of $N(\mathrm{H\,I})_{\mathrm{abs}}$ in the CNM ($T_s \leqslant 250$ K). If no CNM components were detected within uncertainties, equal to 0.0. Col. (6): sum of $N(\mathrm{H\,I})_{\mathrm{abs}}$ in the UNM ($250 < T_s \leqslant 1000$ K). If no UNM components were detected within uncertainties, equal to 0.0. Col. (7): CNM fraction per LOS ($f_{\mathrm{CNM}} = N(\mathrm{H\,I})_{\mathrm{CNM}}/N(\mathrm{H\,I})_{\mathrm{total}}$). Col. (8): UNM fraction per LOS ($f_{\mathrm{UNM}} = N(\mathrm{H\,I})_{\mathrm{UNM}}/N(\mathrm{H\,I})_{\mathrm{total}}$).

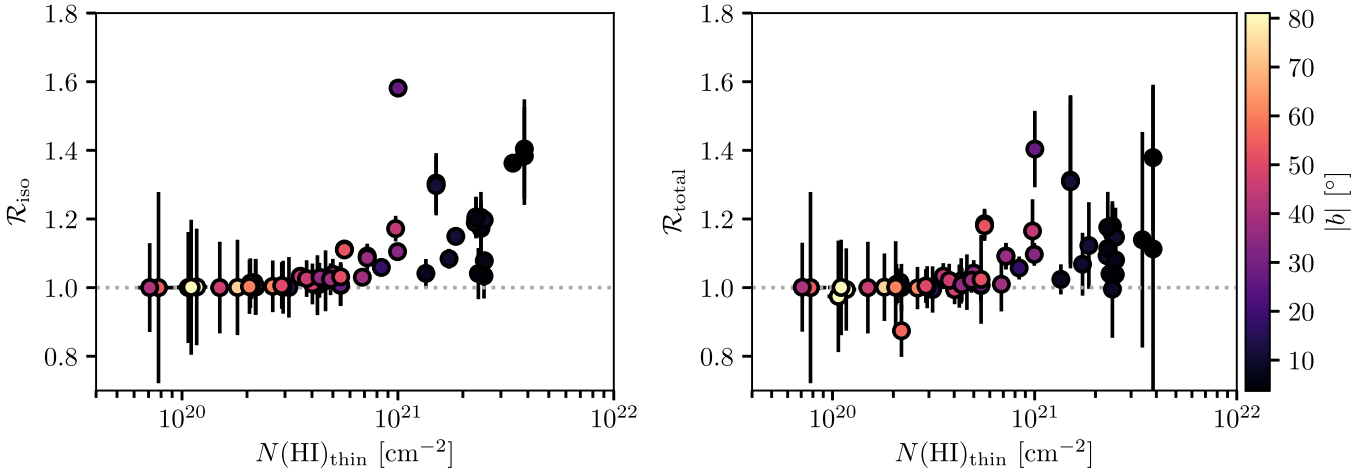

Figure 4. The effect of optical depth on the LOS column density. Left: isothermal column density correction factor ($\mathcal{R}_{\rm iso} = N(\mathrm{H\,I})_{\rm iso}/N(\mathrm{H\,I})_{\rm thin}$) vs. optically thin column density ($N(\mathrm{H\,I})_{\rm thin}$). Right: "total" column density correction factor ($\mathcal{R}_{\rm total} = N(\mathrm{H\,I})_{\rm total}/N(\mathrm{H\,I})_{\rm thin}$) vs. $N(\mathrm{H\,I})_{\rm thin}$. Data points are colored by the absolute Galactic latitude of the LOS ($|b|$).

trials used to estimate the uncertainty in $N(\mathrm{H\,I})_{\rm total}$. Next, we compute upper limits to the column density of CNM and UNM below our sensitivity limit by integrating the uncertainty spectrum ($\sigma_\tau(v)$) and assuming $T_s = 100$ K and $T_s = 500$ K for the CNM and UNM, respectively. The final uncertainty is the maximum value between these two estimates.

Keeping in mind the large uncertainties in the LOS mass fractions, we observe most LOSs are roughly less than or roughly half made up of CNM by mass. This is in agreement with a similar analysis of 21 cm absorption line pairs within and around the Perseus molecular cloud (Stanimirović et al. 2014), and also with HT03. All LOSs feature a significant fraction of WNM by mass, detected only in emission. We will return to discuss the overall mass fractions in the CNM, UNM, and WNM in Section 6.

In Figure 5 we plot $f_{\rm CNM}$, versus the optical-depth-weighted harmonic mean spin temperature, $\langle T_s \rangle$, given by

$$\langle T_s \rangle = \frac{\int \tau(v) \cdot T_s(v)\, dv}{\int \tau(v)\, dv} = \frac{\int \tau(v) \cdot \frac{T_B(v)}{(1-\exp(-\tau(v))}\, dv}{\int \tau(v)\, dv}. \quad (10)$$

Although the uncertainty in $f_{\rm CNM}$ is large, the observed data points cluster around a relation given by $f_{\rm CNM} = T_s/\langle T_s \rangle$ for $T_s = 77 \pm 57$ K (corresponding to the mean and standard deviation of T_s for the CNM). This behavior is consistent with previous observational results (Stanimirović et al. 2014; Murray et al. 2015), as well as with KOK14, and suggests that $\langle T_s \rangle$ may be used as an alternative tracer for $f_{\rm CNM}$. Future observations at high latitude, where minimal line blending reduces the uncertainty in parameter decomposition, will be important for testing this hypothesis further.

In Figure 6, we plot the all-sky distributions of $f_{\rm CNM}$ (top), $f_{\rm UNM}$ (middle), and $\langle T_s \rangle$ (bottom). The highest Galactic latitudes are dominated by WNM (generally low $f_{\rm CNM}$ and $f_{\rm UNM}$), whereas low Galactic latitudes feature the largest $f_{\rm CNM}$. Sight lines with the largest $\langle T_s \rangle$, as shown in Figure 5, feature small $f_{\rm CNM}$ and intermediate $f_{\rm UNM}$.

We explore the effect of interstellar environment further in Figure 7, where we compare $\langle T_s \rangle$ with dust temperature $T_{d,\rm Planck}$, derived from modified blackbody fits to *Planck* observations at 353, 545, and 857 GHz, as well as to *IRAS*

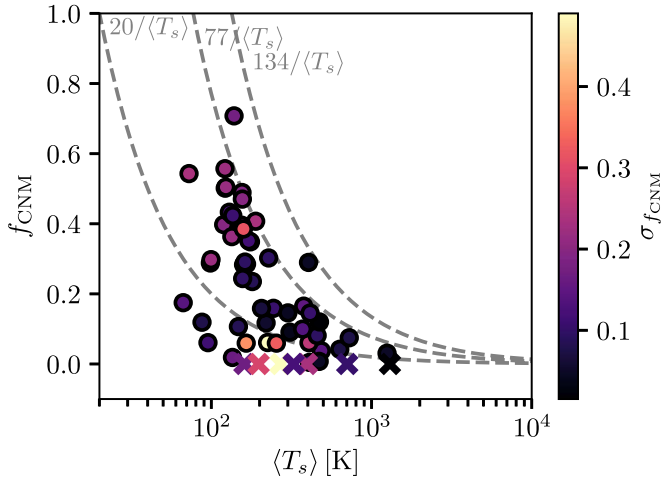

Figure 5. Optical-depth-weighted average spin temperature along the LOS ($\langle T_s \rangle$) vs. CNM fraction ($f_{\rm CNM}$). Dashed lines denote $T_s/\langle T_s \rangle$ for $T_s = 77 \pm 57$ K (the mean $\pm$ the standard deviation T_s for the CNM). Crosses indicate LOSs with $f_{\rm CNM} = 0$, and points are colored by the uncertainty in $f_{\rm CNM}$ ($\sigma_{f_{\rm CNM}}$). Despite the large scatter, as the majority of observed data points are consistent with the dashed lines, this suggests that $\langle T_s \rangle$ may be used as a tracer of $f_{\rm CNM}$.

100 μm emission (Planck Collaboration et al. 2014). The dust temperature is a first-order approximation of the interstellar radiation field, which will affect the neutral gas temperature distribution. There is considerable scatter within a narrow range of observed $T_{d,\rm Planck}$; however, there is a very weak discernible linear trend ($p = 0.005$) of increasing $\langle T_s \rangle$ with increasing $T_{d,\rm Planck}$, illustrated by the mean and standard deviation $T_{d,\rm Planck}$ in bins of increasing $\langle T_s \rangle$ (red crosses). In agreement, Kalberla & Haud (2018) observed that $T_{d,\rm Planck}$ decreases in regions dominated by the CNM, which correspond to low $\langle T_s \rangle$. Taken together with the trends observed in Figure 6, this provides tentative evidence that stronger interstellar radiation fields result in smaller CNM fractions.

5.1. Mass Distribution of H I as a Function of T_s

In Figure 8, we display a histogram (top panel) and CDF (bottom panel) of the fraction of the total column density detected in absorption and emission over all LOSs per T_s bin

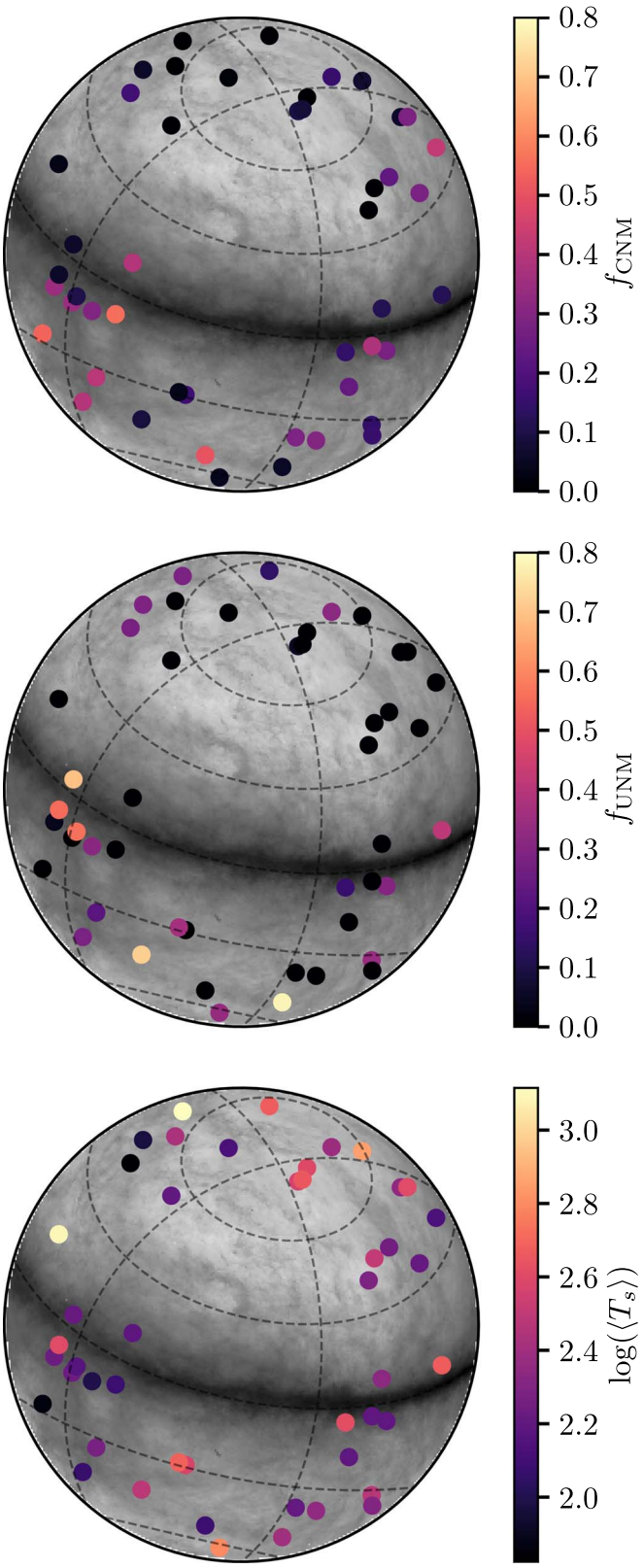

Figure 6. All-sky plots of CNM fraction ($f_{\rm CNM}$; left), UNM fraction ($f_{\rm UNM}$; right), and optical depth-weighted harmonic mean spin temperature ($\langle T_s \rangle$; right), overlaid on H I column density maps in ZEA projection from EBHIS (Winkel et al. 2016).

$(d\,N\,({\rm H\,I})/d\,T_s)$, a quantity that we denote the "gas fraction" as a function of spin temperature. In the bottom panel, we include CDFs of the results of M15 (purple dashed) for comparison.

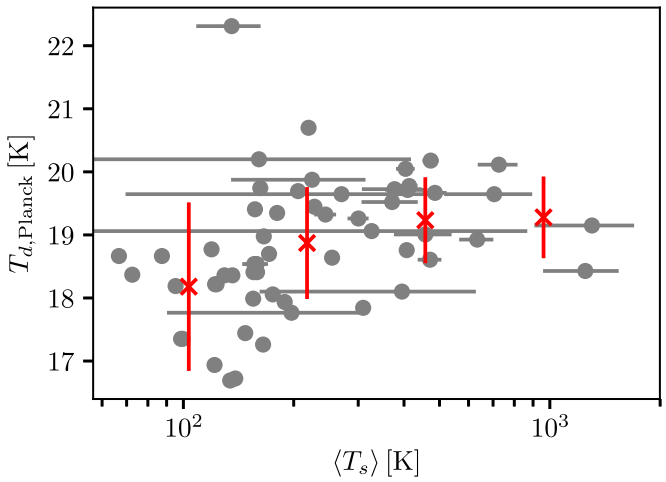

Figure 7. Optical-depth-weighted average spin temperature ($\langle T_s \rangle$) vs. dust temperature ($T_{d,\rm Planck}$). The mean and standard deviation over $T_{d,\rm Planck}$ in bins of increasing $\langle T_s \rangle$ are plotted as red crosses.

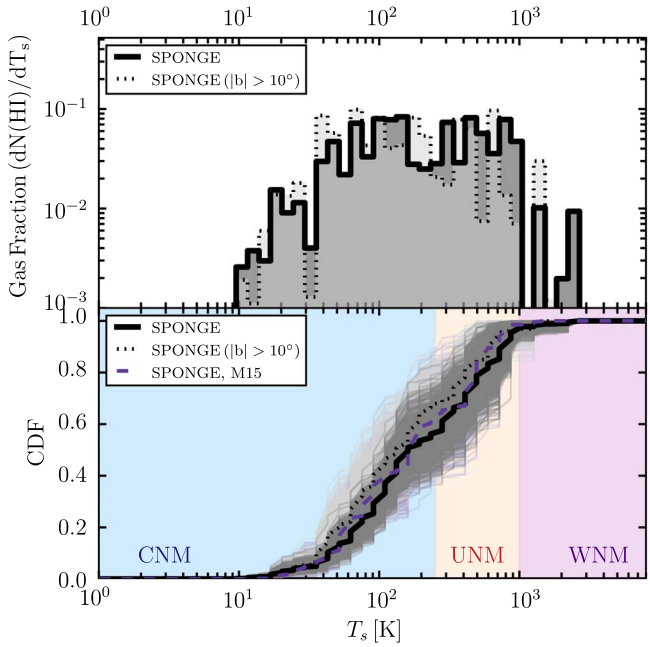

Figure 8. Fraction of total column density detected by 21-SPONGE in absorption as a function of spin temperature for the full sample of 222 absorption components (solid) and the 134 components detected in high-latitude ($|b| > 10°$) LOS (dotted). The results from the first half of the 21-SPONGE survey are shown for comparison (purple dashed; M15). Top: histogram. Bottom: cumulative distribution function (CDF). Approximate spin temperature ranges corresponding to the CNM ($T_s \leqslant 250$ K), UNM ($250 < T_s < 1000$ K), and WNM ($T_s > 1000$ K) are shaded in blue, orange, and purple, respectively.

We bootstrap the observed distributions over 1000 trials and include each resampled CDF to illustrate the effect of outliers on the distribution shapes.

To test the effect of interstellar environment on the observed gas fractions, we isolate the 134 components found at high latitudes ($|b| > 10°$) and include the results for this subsample (black dotted). Sight lines at low Galactic latitude feature increased spectral line complexity due to blending of overlapping structures in radial velocity and also probe different Galactic conditions. We find no significant difference in the observed gas fraction as a function of spin temperature between

Table 3
H I Mass Fractions

Phase	Absorption	Total
CNM	0.56 ± 0.10	0.28
UNM	0.41 ± 0.10	0.20
WNM	0.03 ± 0.05	0.52

Note. To compute the "Absorption" mass fractions, we adopt definitions of each phase as follows: over all bootstrapped trials displayed in Figure 8, the maximum T_s varies between 150 and 350 K (Wolfire et al. 2003, cf. their Table 3), the minimum WNM T_s varies between 1000 and 4000 K (Liszt 2001), and the UNM occupies the intervening T_s. The "Total" mass fractions are computed by incorporating the 50% of the total H I mass detected in emission only, which we assume is WNM.

the full and high-latitude samples. We will discuss this further in Section 6.2.

In Table 3 we list the total mass fractions of gas detected in absorption from each ISM phase in 21-SPONGE. These fractions and their uncertainties were computed as the mean and standard deviation over bootstrapped trials (Figure 8). In each trial, using the range of predicted T_s from Wolfire et al. (2003, cf. their Table 3), we allowed the maximum spin temperature definition of the CNM to vary from $T_s < 150$–350 K and the definition of the WNM to vary from $T_s > 1000$–4000 K (with the UNM defined as the intervening temperatures) to incorporate the uncertainty in these definitions. We also include the fractions of the total H I column density in each phase, with the assumption that the 50% of the total H I column density detected by 21-SPONGE in emission alone is from the WNM.

5.2. Estimating Observational Bias

To address the bias imposed by our analysis method on the observed 21-SPONGE mass distribution (i.e., bias toward certain spectral line shapes imposed by AGD, or observational sensitivity limits), we compare H I mass distributions from simulated data. First, in an identical manner to the 21-SPONGE distributions shown in Figure 8, we compute the fraction of total column density in each T_s bin from the Gaussian decomposition of the 9355 synthetic spectral line pairs from KOK14 with maximum WF. For each LOS, we then extract the density (n) and temperature (T) as a function of distance (s) from the KOK13 simulation used to construct the synthetic spectra in KOK14. To compare with the "observed" mass distribution of H I as a function of T_s, we estimate the "true" underlying mass distribution by computing the fraction of total n per T_s bin for all gas along the KOK13 simulated LOS from which the KOK14 spectra were computed. We display both distributions in the top panel of Figure 9.

To emphasize the influence of the WF prescription on these results, in the top panel of Figure 9, we also include the mass distribution as a function of T_s from the KOK13 simulation under the assumption of a constant Lyα radiation field density (10^{-6} cm^{-3}; dashed blue) for comparison. Although the mass fractions in the CNM are unchanged between the "constant" and "maximum" WF effect implementation, the peak of the WNM spin temperature distribution changes from ∼4000 to ∼6000 K. Clearly, the implementation of the WF effect has the potential to change the WNM spin temperature distribution dramatically.

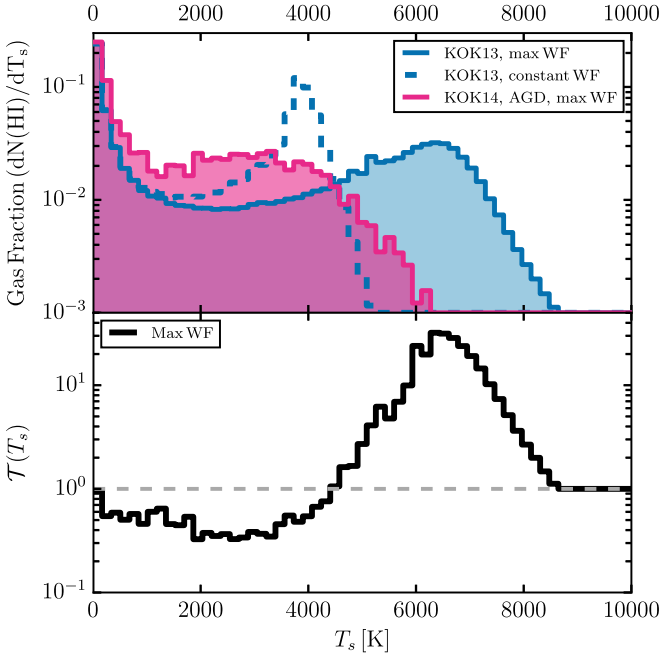

Figure 9. Top: fraction of total column density as a function of spin temperature computed from the KOK13 simulation with maximum WF (i.e., $T_s = T_k$; solid blue), with constant WF (dashed blue), and from the AGD analysis of KOK14 (pink). Bottom: transfer function, $\mathcal{T}(T_s)$, derived by comparing the temperatures and densities of ISM simulated by KOK13 with those inferred from the synthetic observations of KOK14 (Equation (12)).

By comparing the KOK13 and KOK14 distributions in Figure 9 (with max WF) in detail, we can quantify the differences between observed and simulated H I mass distributions. Specifically, we compute a "transfer function," $\mathcal{T}(T_s)$, where

$$\left(\frac{d\,N(\mathrm{H\,I})}{d\,T_s}\right)_{\mathrm{true}} = \mathcal{T}(T_s)\cdot\left(\frac{d\,N(\mathrm{H\,I})}{d\,T_s}\right)_{\mathrm{obs}}. \quad (11)$$

Assuming that KOK13 and KOK14 trace the "true" and observed gas fractions respectively, we have

$$\mathcal{T}(T_s) = \left(\frac{d\,N(\mathrm{H\,I})}{d\,T_s}\right)_{\mathrm{KOK13}} \Bigg/ \left(\frac{d\,N(\mathrm{H\,I})}{d\,T_s}\right)_{\mathrm{KOK14,AGD}}. \quad (12)$$

We display $\mathcal{T}(T_s)$ for all bins with $dN(\mathrm{H\,I})/dT_s > 0.001$ in the bottom panel of Figure 9. The shape of the transfer function encodes biases in our AGD-based analysis method's recovery of a realistic H I mass distribution. In addition, $\mathcal{T}(T_s)$ encodes the radiative transfer and WF prescription required to go from (n, T_k) in KOK13 to synthetic spectra in KOK14, as well as observational sensitivity limitations imposed by adding synthetic noise to the KOK14 spectra. We emphasize that $\mathcal{T}(T_s)$ will be used in this work to qualitatively assess these limitations. In the future, a full library of simulations and synthetic observations is required to find the best fit with observations and to correct observed gas fractions quantitatively.

6. Discussion

With the preceding analysis in hand, we will discuss the observed properties of Galactic H I from 21-SPONGE, aided by the concurrent analysis of synthetic 21 cm spectral lines from numerical simulations. As numerical simulations produce models of the ISM with increasing resolution, precision, and

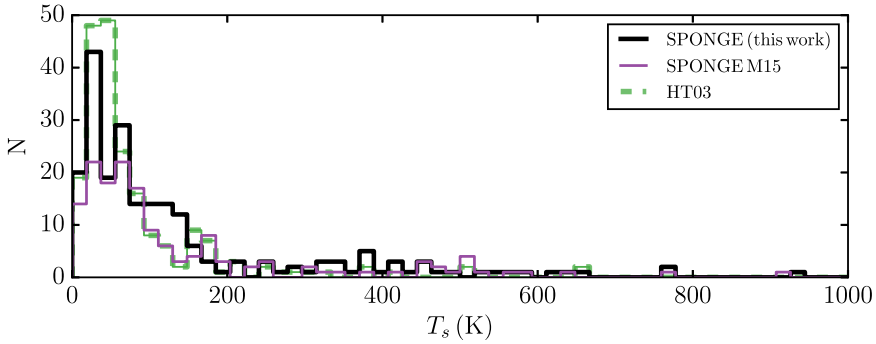

Figure 10. Histogram of spin temperatures (T_s) for components with $T_s \leqslant 1000$ K from 21-SPONGE (57 LOS; thick black), the first half of the 21-SPONGE survey (M15; thin purple), and HT03 (79 LOS, dashed green). The higher sensitivity of 21-SPONGE has the effect of broadening the T_s distribution for the CNM ($T_s \lesssim 200$ K).

accuracy, and as wide field surveys at next-generation observatories roll in, this is likely to become an increasingly common practice. We emphasize that the AGD-based decomposition and radiative transfer approach presented here was designed to be applied to real and synthetic data volumes which are too large to analyze by hand, so that this study may serve as a pilot for future surveys.

So, what have we learned from 21-SPONGE? In this section, we discuss salient properties of the three canonical H I phases, the CNM, UNM, and WNM.

6.1. The CNM is Ubiquitous

Of all the H I phases, we are most successful in recovering the physical properties of the CNM. From a detailed comparison between individual clouds along simulated KOK13 LOSs and decomposed spectral features from KOK14 synthetic spectra, we demonstrated that our spectral analysis method not only recovers the majority of "real" CNM clouds, but successfully infers their column densities and spin temperatures (Murray et al. 2017). Furthermore, we observe that the transfer function in Figure 9 is ∼1 in the CNM regime at low T_s, indicating that our the AGD-plus-radiative transfer method is relatively complete in its recovery of the overall fraction of H I mass in the CNM.

21-SPONGE has established that with improved sensitivity in optical depth, signatures of the CNM in the form of weak, narrow absorption lines are detected ubiquitously. This agrees with Stanimirović & Heiles (2005), who found that increased integration time on several nondetection sight lines from HT03 revealed CNM absorption features. Out of 57 total LOSs, we have only 7 nondetections of the CNM (∼88% detection rate). For five of these sources (3C 236, 3C 245B, 4C 25.43, J1613, 3C 345), no absorption was detected above $3\sigma_\tau(v)$, and for two sources (3C 245A, 1055+018), no detected components featured $T_s \leqslant 250$ K within uncertainties from the AGD-based fit. Furthermore, we detect the majority of H I mass in absorption from the CNM, 56% ± 10% (28% of the total H I mass including WNM detected only in emission).

However, despite the ubiquity of the CNM, the integrated optical depths are low enough that the correction to the total column density for the presence of cold, optically thick H I is relatively small. As shown in Figure 4, it is only sources at low Galactic latitudes ($|b| \lesssim 10°$) that exhibit correction factors significantly greater than unity. Our results agree with previous studies of 21 cm absorption to infer the optical depth correction to the H I column density budget (Heiles & Troland 2003a; Lee et al. 2015; Reach et al. 2017; Nguyen et al. 2018). For example, Lee et al. (2015) analyzed 26 sight lines within and around the Perseus molecular cloud to estimate the contribution of optically thick H I to the "dark gas" budget (i.e., gas undetected in H I or CO emission). Applying a trend similar to that observed in Figure 4, they found that the total H I mass of Perseus increases by only 10% due to optically thick H I. Together, our results contrast recent studies inferring significant corrections (≳200%) to the total gas column density from optically thick H I based on observed far-infrared properties of dust (e.g., Fukui et al. 2015) and indicate that optically thick H I is not likely a dominant component of CO-dark gas in the local ISM (Murray et al. 2018).

To compare with previous studies of CNM properties, in Figure 10 we display histograms of T_s below 1000 K from 21-SPONGE (thick black), M15 (thin purple), and HT03 (dashed green). The HT03 distribution is strongly peaked at ∼50 K, indicative of a characteristic T_s for the CNM. Although we observe a similar feature in 21-SPONGE, we also find evidence for a broader CNM T_s distribution. To compare the statistics in detail, in Table 4 we compute mean and median values for the CNM T_s from 21-SPONGE and HT03 (i.e., all components with $T_s \leqslant 250$ K) with and without weighting by $N(\mathrm{H\,I})_{\rm abs}$ for two latitude bins, above and below $|b| = 10°$, following Table 2 of Heiles & Troland (2003b). Considering the scatter (standard deviations ≳50 K), the values are generally consistent. We appear to detect higher mean and median CNM T_s weighted by $N(\mathrm{H\,I})_{\rm abs}$ in 21-SPONGE than HT03, consistent with the observed broadening of the T_s histogram in Figure 10.

Ultimately, improving the statistics of the CNM T_s distribution will be crucial for understanding the sources of observed differences and scatter between distributions, as environmental effects are likely important. For example, photoelectric heating by dust grains may be enhanced in particularly dust-rich Galactic environments, or strong variations in turbulence may broaden the distribution. Upcoming 21 cm absorption surveys at the VLA and Australian Square Kilometer Array Pathfinder (GASKAP; Dickey et al. 2013) will dramatically expand the known sample of Galactic H I absorption properties. Although these studies will likely not reach the optical depth sensitivity in individual sight lines achieved by 21-SPONGE, they will be crucial for resolving detailed CNM properties as a function of Galactic environment.

Table 4
CNM and UNM T_s Statistics

Latitude	Survey	N_{CNM}	By N_{CNM} (K)		By N(H I) (K)		N_{UNM}	By N_{UNM} (K)		By N(H I) (K)	
			Mean	Median	Mean	Median		Mean	Median	Mean	Median
High	21-SPONGE	109	73	61	95	79	23	450	390	500	460
($\|b\| > 10°$)	HT03	135	63	45	74	56	11	420	380	400	380
Low	21-SPONGE	71	68	49	108	106	14	460	430	510	490
($\|b\| < 10°$)	HT03	51	67	47	86	60	2	300	300	260	260

Note. Means and medians "by N" are computed for all N_{CNM} CNM components ($T_s \leqslant 250$ K) and all N_{UNM} UNM components ($250 \leqslant T_s \leqslant 1000$ K) with no weighting; following Heiles & Troland (2003b), the median "by N(H I)" is the T_s for which half the total CNM or UNM column density lies above and half below, and the mean is weighted by N(H I).

6.2. Thermally Unstable Gas Fraction

A key motivation for the 21-SPONGE survey was to determine the effect of improved optical depth sensitivity on the inferred fraction of H I mass in the thermally unstable regime (e.g., $250 \lesssim T_s \lesssim 1000$ K). There is substantial evidence in the literature for a significant population of thermally unstable gas in the ISM; however, the majority of constraints on unstable spin temperatures are inferred as upper limits from line-width-based kinetic temperatures (e.g., Verschuur & Magnani 1994; Heiles & Troland 2003a; Haud & Kalberla 2007; Kalberla & Haud 2018). With detections in τ and T_B, we can constrain T_s and more accurately assess the thermodynamic state of the neutral ISM.

However, as spectral features corresponding to warmer gas are characterized by broader line widths, spectral complexity due to velocity blending increases the difficulty in recovering accurate gas density and temperature from both 21 cm absorption and emission. We quantified this effect in Murray et al. (2017) by showing that our decomposition and radiative transfer approach tends to overestimate the temperatures of non-CNM structures ($T_s \gtrsim 400$ K). In that study, we were primarily sensitive to gas with $T_s < 1000$ K (i.e., CNM and UNM) for which we could unambiguously identify "true" simulated counterpart structures along the simulated LOS. Considering this bias, the mass fraction of thermally unstable H I in absorption presented here is possibly an upper limit, as CNM with overestimated T_s may contribute. We also note that in the expected range of thermally unstable temperatures ($250 \lesssim T_s \lesssim 1000$ K), we observe that $\mathcal{T}(T_s)$ is relatively flat but <1 (Figure 9), indicating that our analysis method is not only sensitive to these conditions but that we tend to overestimate the true mass fraction.

To illustrate the typical UNM properties detected by 21-SPONGE (in comparison with HT03), in Table 4 we display mean and median values for the UNM T_s from 21-SPONGE and HT03 (i.e., all absorption components with $250 < T_s < 1000$ K) with and without weighting by $N(\mathrm{H\,I})_{abs}$ for high and low Galactic latitudes. The statistics are much poorer for comparing UNM properties (i.e., HT03 only find two UNM components at low latitudes, due to limited observational sensitivity); however, the observed UNM properties appear to be largely consistent with each other at both high and low latitudes.

Our estimate of the thermally unstable gas fraction (41% $\pm$ 10% of H I detected in absorption by mass, and ~20% of the total observed H I mass) is generally consistent with previous observational results. Although Kalberla & Haud (2018) find a larger UNM fraction—41% of the local H I mass—they acknowledge that the systematic uncertainties on this estimate are likely very large, up to 50%. As discussed above, identifying spectral features from the UNM is complicated by uncertainties in the definition of CNM and WNM thresholds, and the fact that the UNM is typically strongly blended with CNM and WNM features. Furthermore, to distinguish between disparate H I phases using 21 cm emission and $T_{k,max}$ alone requires uncertain assumptions regarding the contributions of thermal and nonthermal broadening to the observed line widths. Without sufficient observational sensitivity to detect UNM consistently in 21 cm absorption, HT03 determined that ~48% of the total WNM column density beyond the Galactic plane, or ~30% of the total out-of-plane column density, has thermally unstable temperatures. For comparison with our UNM fraction, of the gas detected in absorption by HT03, only 9% by mass has $250 \leqslant T_s < 1000$ K. With improved 21 cm absorption sensitivity, a study by Roy et al. (2013b) similar to 21-SPONGE argued that at least 28% of H I is thermally unstable. Finally, KOK13 also find a substantial fraction of gas out of thermal equilibrium, ~18% by mass, due to strong turbulence, expanding shocks from supernovae, and a time-dependent heating rate. Below $T_s \sim 1000$ K, our observed distribution qualitatively agrees with their results (cf. Figure 8(d) of KOK13).

In contrast to HT03, we do not observe a significant difference between the mass distribution of H I (including the thermally unstable gas fraction) between the full sample and subsample of sight lines at high Galactic latitude ($|b| > 10°$). Considering that velocity blending and overall fitting uncertainties are higher at lower latitudes, we might expect some kind of bias toward certain gas populations in different regimes. To resolve variations with Galactic environments, we need larger samples of high-sensitivity absorption lines to improve statistics, which may distinguish between regimes where thermal instability, turbulence, and dynamical processes dominate the regulation of the ISM (Wolfire 2015).

6.3. How "Warm" is the WNM?

From standard, steady-state ISM models, we expect the WNM to have kinetic temperatures of $T_k = 5000$–10000 K and spin temperatures of $T_s \sim 1000$–4000 K (Liszt 2001; Wolfire et al. 2003). In the WNM, it is typically assumed that $T_s < T_k$ because collisions are insufficient at low densities for thermalizing the 21 cm transition. Our AGD analysis of KOK14 spectra demonstrates that we should easily detect WNM in the expected range of spin temperature, despite the limitations of our observational sensitivity. The prominent peak at $T_s \sim 2500$ K in the KOK14 histogram of Figure 8 (pink) illustrates the sensitivity of the AGD method to this range of temperature. However, we detect very little H I mass in absorption from the WNM (3% $\pm$ 5%).

Consequently, the fact that we do not detect a significant mass fraction of WNM from 21-SPONGE with $T_s \gtrsim 1000$–4000 K

indicates that the WNM spin temperature may be higher than standard analytical predictions, which are based on H I excitation via particle collisions alone (e.g., Liszt 2001). In agreement, Murray et al. (2014) detected an unexpectedly "warm" WNM population with $T_s = 7200^{+1800}_{-1200}$ K, which was attributed to supplemental excitation beyond collisions from resonant scattering of Lyα photons (the WF effect; Wouthuysen 1952; Field 1958). In Murray et al. (2017), we found that a simple WF treatment in KOK14 spectra produces spectral features corresponding to expected WNM properties (i.e., $T_s \sim$ 3000–4000 K), but which are not detected by 21-SPONGE, and this comparison is what led us to analyze synthetic spectra from KOK14 with "maximum WF" in this study. Sophisticated theoretical treatment of the WF effect in future simulations is of utmost importance, as myriad environmental conditions, including metallicity and cosmic-ray ionization rate, will affect Lyα pumping of the 21 cm transition (e.g., Shaw et al. 2017).

Ultimately, considering that we analyze the "maximum" WF case of the KOK14 synthetic spectra ($T_s = T_k$ for all H I), we are likely limited by observational sensitivity to detecting gas at higher spin temperatures (i.e., $T_s \gtrsim 4000$ K: prominent in the KOK13 mass distribution but missing from the inferred distribution from KOK14). We added synthetic Gaussian noise with rms $= 1 \times 10^{-3}$ to the synthetic absorption spectra from KOK14 to mimic the 21-SPONGE sensitivity, and AGD is unable to recover lines with $T_s \gtrsim 4000$ K at S/N $\geqslant 3$ with this level of spectral uncertainty. As a result, the majority of H I mass not detected in absorption (50% of the total LOS column density) is likely in the form of WNM.

To test for the presence of WNM below our sensitivity limit, we performed a simple stacking experiment. First, we subtracted all components detected in both absorption and emission from $\tau(v)$ and $T_{B,\mathrm{exp}}(v)$ to produce residual absorption and emission spectra, $\tau_{\mathrm{resid}}(v)$ and $T_{B,\mathrm{exp,resid}}(v)$, for all LOSs. The residual spectra contain components with unphysical T_s (i.e., not successfully fitted to $T_{B,\mathrm{exp}}(v)$) and H I below our sensitivity limit to detect in absorption (i.e., WNM at high temperature). We mask all velocity channels with components detected in $\tau(v)$ but not $T_{B,\mathrm{exp}}(v)$, as these features are likely CNM or UNM, which we did not recover due primarily to beam mismatch effects. We further mask by eye channels with strong residuals due to the oversubtraction of Gaussian components (typically $\sim$10 channels for roughly half of the LOS). Next, we compute the average of all unmasked velocity channels whose $T_{B,\mathrm{resid}}$ falls into one of four bins (chosen to select significantly detected residual emission in bins of roughly equal sizes), $3\sigma_{T_B} \leqslant T_{B,\mathrm{exp,resid}} < 0.9$ K, $0.9 \leqslant T_{B,\mathrm{exp,resid}} < 2.4$ K, and $T_{B,\mathrm{exp,resid}} > 2.4$ K, weighted by $1/\sigma_\tau$. The number of channels in each bin is 2383, 2604, and 2423, respectively, from low to high $T_{B,\mathrm{exp,resid}}$. In Figure 11, we plot the resulting weighted averages of the absorption channels, $\langle 1 - e^{-\tau_{\mathrm{resid}}(v)} \rangle$, and the emission channels $\langle T_{B,\mathrm{exp,resid}} \rangle$. The weighted average absorption in the bins of smallest $T_{B,\mathrm{exp,resid}}$ is consistent with zero; however, we detect a significant residual absorption signal in the bin of highest $T_{B,\mathrm{exp,resid}}$. The uncertainties are computed as the standard deviation over 10^4 trials wherein we bootstrap-resample the LOS used in the stack with replacement. We denote the constant harmonic mean T_s ($\langle T_{s,\mathrm{resid}} \rangle$) with dotted lines and shading in Figure 11, and observe that the significant residual absorption feature is consistent with $\langle T_{s,\mathrm{resid}} \rangle \sim 10^4$ K.

The inferred spin temperature of the detected residual absorption signal in Figure 11 is consistent with our previous findings

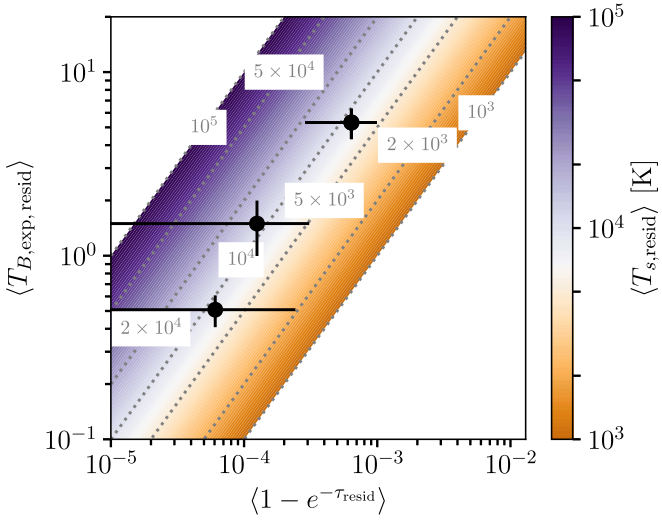

Figure 11. Stacked residual absorption $\langle 1 - e^{-\tau_{\mathrm{resid}}} \rangle$ vs. stacked residual emission $\langle T_{B,\mathrm{resid}} \rangle$ for all spectral channels binned by residual emission: $3\sigma_{T_B} \leqslant T_{B,\mathrm{resid}} < 0.9$ K, $0.9 \leqslant T_{B,\mathrm{resid}} < 2.4$ K, and $T_{B,\mathrm{resid}} > 2.4$ K (limits chosen to select significantly detected residual emission in three bins of roughly equal sizes). Dotted gray lines, shading, and inset labels denote constant harmonic mean spin temperature for the stacked residual channels ($\langle T_{s,\mathrm{resid}} \rangle$). For the bin of largest residual emission, we detect a significant residual absorption signal, corresponding to $\langle T_{s,\mathrm{resid}} \rangle \approx 10^4$ K.

($T_s = 7200^{+1800}_{-1200}$ K; Murray et al. 2014). Although we do not detect a significant signal in the bins of smallest $T_{B,\mathrm{resid}}$, possibly due to oversubtraction of Gaussian components in complex LOSs, we note that the mean $\langle T_{s,\mathrm{resid}} \rangle$ is similar in all bins. This is expected if we are sampling broad spectral line features from a diffuse, warm parent H I population, rather than randomly sampling occasional peaks in T_B or τ due to fitting imperfections. If the signal detected here (and in Murray et al. 2014) originates from the diffuse WNM with a constant temperature, bins of higher $T_{B,\mathrm{resid}}$ should correspond to higher $(1 - e^{-\tau_{\mathrm{resid}}})$.

Overall, the detection of a residual absorption signal consistent with high WNM spin temperature further emphasizes the importance of supplementary diffuse neutral gas excitation (e.g., the WF effect) in producing such high T_s. In addition, future studies aiming to detect the absorbing properties of the WNM will need to target even better optical depth sensitivity than we have achieved with 21-SPONGE or to improve sensitivity by applying stacking techniques similar to those demonstrated in Figure 11 and by Murray et al. (2014).

7. Summary

In this work, we present the data release of 21-SPONGE, a large Karl G. Jansky VLA survey for high-sensitivity absorption by Galactic H I to probe the temperature distribution of the neutral ISM. 21-SPONGE is distinguished among previous 21 cm studies of the Galactic H I as a result of (1) exceptional optical depth sensitivity ($\sigma_\tau < 10^{-3}$ per 0.42 km s^{-1} channel) thanks to careful calibration considerations and the upgraded capabilities of the VLA WIDAR correlator for producing wide spectral bandwidths and narrow velocity channels for resolving the CNM, UNM, and WNM simultaneously; (2) matching single-dish 21 cm emission spectra with the highest possible angular resolution ($\sim$4′) from the Arecibo Observatory, minimizing the mismatch with sub-arcminute interferometric VLA absorption measurements; and (3) detailed comparisons with 3D numerical simulations of the ISM for assessing observational biases. In this work, we have

presented a novel method for autonomously decomposing 21 cm absorption and emission spectra and deriving the physical properties (column density, temperature) for individual spectral features via detailed radiative transfer. The efficient, objective nature of the analysis method enables us to compare our results with thousands of synthetic observations from numerical simulations. Our main results are summarized here.

1. We demonstrate that with improved optical depth sensitivity, narrow absorption lines arising from the CNM are detected ubiquitously. The detection rate of 21 cm absorption from the CNM is ∼88%. However, the optical depth of these features is typically small so that correction for cold, optically thick gas to the optically thin limit of H I column density is typically small (<20%). Along a typical individual 21-SPONGE LOS, we find the CNM mass fraction to be $\lesssim$50%.
2. To assess the biases of our observational methods, we apply the same analysis techniques to a sample of 9355 synthetic H I spectral line pairs from Kim et al. (2014), constructed from the 3D hydrodynamical simulation by Kim et al. (2013). We add spectral noise to the synthetic data set to mimic the 21-SPONGE sensitivity limits. By comparing the underlying simulated gas properties with those inferred from the synthetic spectral lines, we construct a "transfer function," $\mathcal{T}(T_s)$, between the true and observed mass distributions of H I as a function of temperature (i.e., by dividing the two distributions). We find that for $T_s < 4000$ K, $\mathcal{T}(T_s) \sim 1$, indicating that we are sensitive to H I properties within this regime. At higher T_s (i.e., $\gtrsim$4000 K), $\mathcal{T}(T_s) > 1$, indicating that our synthetic spectral line analysis is likely missing a significant fraction of WNM mass present in the KOK13 simulation.
3. We compute the fractions of H I mass detected in emission and absorption (i.e., for which we have constraints on T_s for measuring N(H I), corresponding to 50% of the total H I mass) in the CNM (56% ± 10%), WNM (3 ± 5%), and thermally unstable medium (UNM; 41% ± 10%). Our UNM mass fraction, among the first observational constraints from direct H I absorption detections, is generally consistent with previous indirect observational estimates (e.g., Heiles & Troland 2003b). Incorporating the remaining 50% of H I mass detected in emission alone (i.e., for which we do not have constraints on T_s, which we assume is due to WNM), for all 21-SPONGE LOSs, the total mass fractions are 28%, 20%, and 52% for the CNM, UNM, and WNM, respectively.
4. Although the WNM makes up the majority of the total H I mass (52%), the lack of WNM absorption detected by 21-SPONGE in the spin temperature range expected from steady-state collisional excitation models (T_s = 1000–4000 K; Liszt 2001; Wolfire et al. 2003) implies that the WNM spin temperature is higher, likely due to supplemental excitation from the WF effect. This is in agreement with previous analysis of 21-SPONGE and the KOK14 synthetic spectra (Murray et al. 2017), as well as stacking analysis of 21-SPONGE spectra, which revealed a high spin temperature WNM population with $T_s = 7200^{+1800}_{-1200}$ K (Murray et al. 2014). As a test of this hypothesis, following spectral line modeling, we stack residual absorption in bins of residual emission and detect a significant absorption feature with a harmonic mean spin temperature $\sim 10^4$ K.

Overall, larger samples of 21 cm absorption lines, as well as next-generation simulations with sophisticated WF treatment, are required to improve the statistical uncertainties and probe the effect of Galactic environment on these results. We emphasize that the autonomous, efficient nature of the AGD method presented here will enable detailed analysis of future real and synthetic data volumes which will be orders of magnitude larger than 21-SPONGE. However, even in the era of next-generation interferometers (e.g., SKA), future surveys will be unlikely to target the superb optical depth sensitivity reached by 21-SPONGE (e.g., McClure-Griffiths et al. 2015), ensuring that this data set will provide an important benchmark for future work.

This work was supported by the NSF Early Career Development (CAREER) Award AST-1056780. C.E.M. acknowledges support by the National Science Foundation Graduate Research Fellowship and the Wisconsin Space Grant Institution. S.S. thanks the Research Corporation for Science Advancement for their support. The authors would like to thank Bob Lindner and Carlos Vera-Ciro for developing AGD, writing GaussPy, and inspiring the methods presented here. C.E.M. thanks Elijah Bernstein-Cooper, Helga Dénes, Katie Jameson, James Dempsey, and Naomi McClure-Griffiths for helpful conversations and collaboration toward developing GaussPy. We also thank Van Hiep Nguyen and Joanne Dawson for valuable discussions that led to improved beam efficiency considerations for our expected brightness temperature spectra. This work makes use of data from the Karl G. Jansky Very Large Array, operated by the National Radio Astronomy Observatory (NRAO). NRAO is a facility of the NSF operated under cooperative agreement by Associated Universities, Inc. EBHIS is based on observations with the 100 m telescope of the MPIfR (Max-Planck-Institut für Radioastronomie) at Effelsberg. The Parkes Radio Telescope is part of the Australia Telescope, which is funded by the Commonwealth of Australia for operation as a National Facility managed by CSIRO. We acknowledge the use of the Legacy Archive for Microwave Background Data Analysis (LAMBDA), part of the High Energy Astrophysics Science Archive Center (HEASARC). HEASARC/LAMBDA is a service of the Astrophysics Science Division at the NASA Goddard Space Flight Center. This research has made use of the NASA/IPAC Extragalactic Database (NED), which is operated by the Jet Propulsion Laboratory, California Institute of Technology, under contract with the National Aeronautics and Space Administration. This research has made use of NASA's Astrophysics Data System. This research made use of Astropy, a community-developed core Python package for Astronomy (Astropy Collaboration et al. 2013), NumPy (Van Der Walt et al. 2011), and matplotlib, a Python library for publication quality graphics (Hunter 2007).

Appendix

In this appendix we include supplementary figures and tables to illustrate the 21-SPONGE data products.

Figure 12 displays 1.4 GHz continuum images of the 21-SPONGE target fields centered on compact sources selected from the NVSS survey (Condon et al. 1998). Many sources exhibit significantly resolved structures.

Figure 13 displays the results of autonomous Gaussian decomposition of the 57 21-SPONGE LOS. The velocity component parameters and estimates for the physical properties of the associated HI structures for each LOS are included in Table 5.

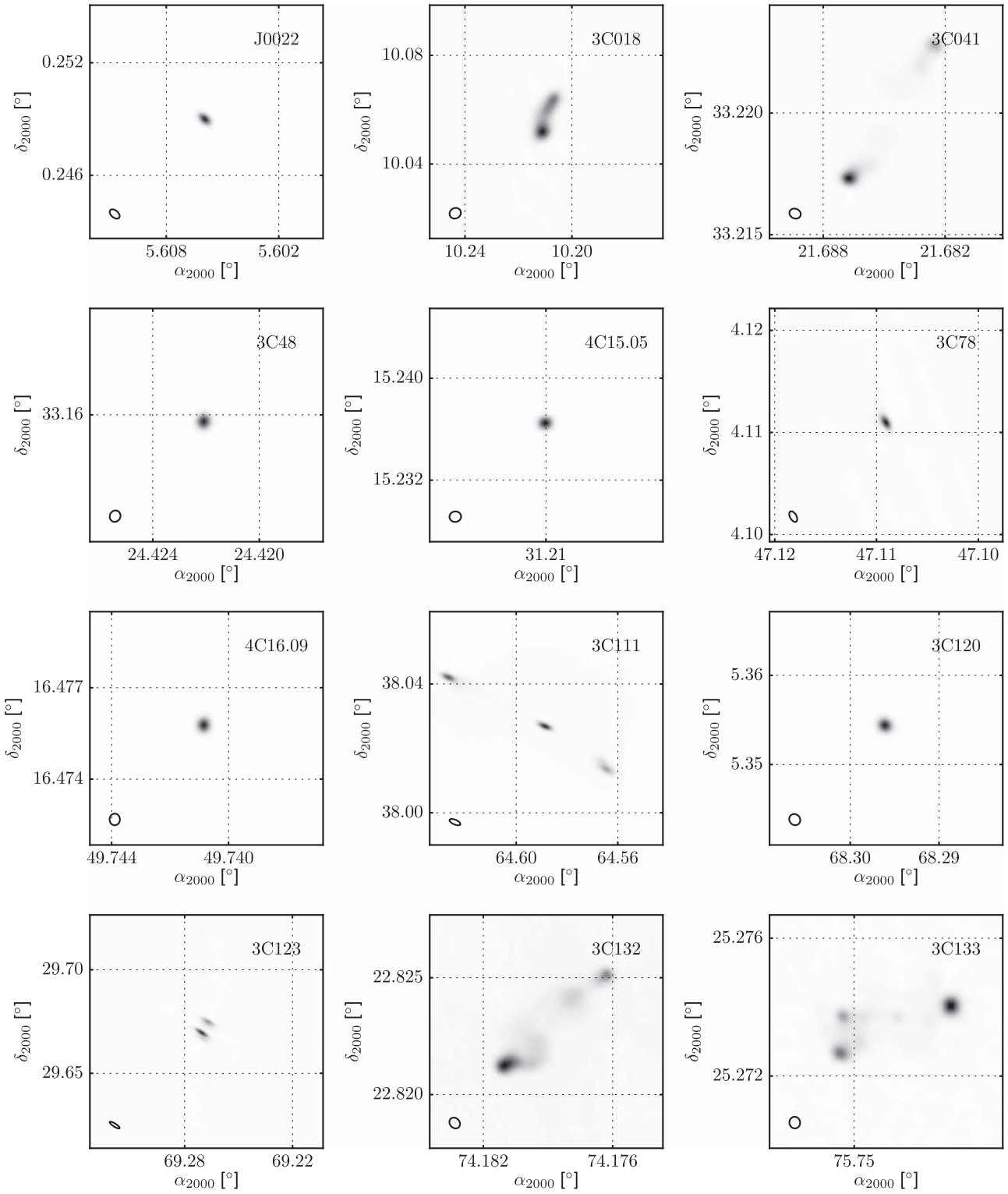

Figure 12. 21-SPONGE 1.42040575 GHz continuum images. The source name is printed within each panel, and the synthesized beam used to construct each image is included in the bottom-left corner. Each image is scaled so that the peak flux density is unity.

(The complete figure set (4 images) is available.)

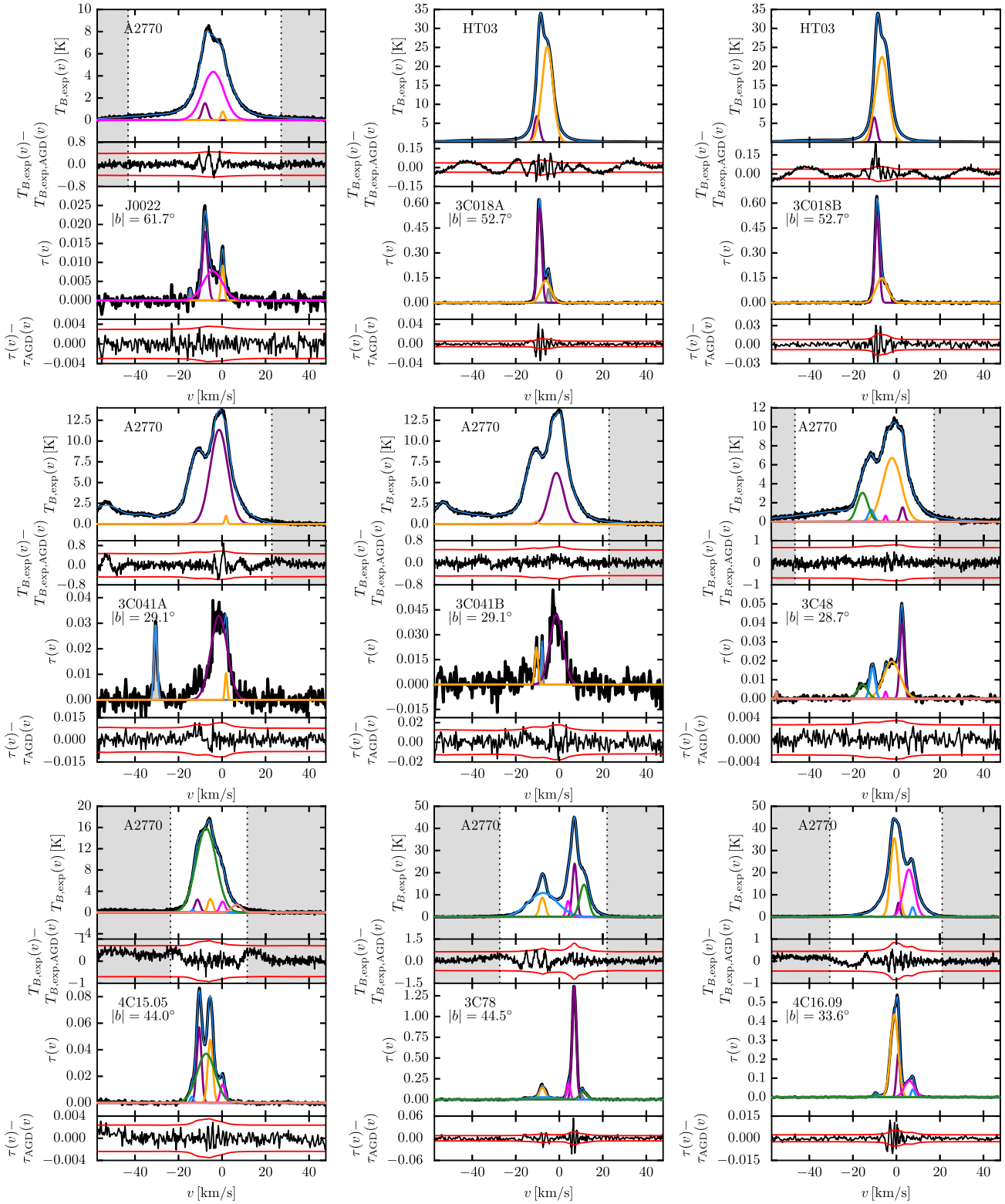

Figure 13. A summary of the Gaussian fits to the 21-SPONGE H I emission and absorption spectral line pairs described in Section 3. In each panel, we plot the emission ($T_{B,\mathrm{exp}}(v)$; top) and absorption ($\tau(v)$; bottom) spectra. The residual spectra following the Gaussian fits are included below each panel, with $\pm 3 \times \sigma_\tau(v)$ and $\sigma_{TB}(v)$, respectively (red). We plot all fitted absorption components in the bottom panel. Components whose derived spin temperatures are unphysical (i.e., $\leqslant$10 K) are plotted in gray, and components with $T_s > 10$ K are plotted in matching colors in the middle and top panels. The total fits, $T_{B,\mathrm{exp,AGD}}(v)$ and $\tau_{\mathrm{AGD}}(v)$, are displayed in thin blue lines. The source of $T_{B,\mathrm{exp}}(v)$, whether from Arecibo (A2770 or HT03) or EBHIS, is printed in the top panels. In the bottom panels, we print the source name and the absolute Galactic latitude ($|b|$). Finally, in the top panels, we shade in gray the velocities where $T_{B,\mathrm{exp}}(v) \leqslant 3 \cdot \sigma_{T_B}(v)$ to illustrate the range over which LOS column densities are computed (i.e., the unshaded region is used). If no vertical shading is present, the full displayed velocity range is used.

(The complete figure set (7 images) is available.)

Table 5
Fitted Parameters

Source (name)	τ_0	Δv_0 (km s^{-1})	v_0 (km s^{-1})	$T_{B,n}$ (K)	$\Delta v_{0,n}$ (km s^{-1})	$v_{0,n}$ (km s^{-1})	T_s (K)	$N(\mathrm{H\,I})_{\mathrm{abs}}$ (10^{20} cm^{-2})	$\mathscr{O}$	$\mathscr{F}$
J0022	0.018 ± 0.001	2.8 ± 0.1	−7.8 ± 0.1	1.5 ± 0.0	3.1 ± 0.1	−7.8 ± 0.1	83 ± 2	0.08 ± 0.00	4	0.0
	0.008 ± 0.001	10.3 ± 0.3	−4.3 ± 0.2	4.4 ± 0.1	11.4 ± 0.1	−4.1 ± 0.1	567 ± 19	0.88 ± 0.05	4	
	0.009 ± 0.001	1.7 ± 0.1	0.3 ± 0.1	0.8 ± 0.0	1.8 ± 0.1	0.3 ± 0.1	84 ± 4	0.03 ± 0.00	4	
	0.003 ± 0.001	1.0 ± 0.2	−14.6 ± 0.1	…	…	…	…	…	…	
3C018A	0.565 ± 0.007	2.5 ± 0.1	−9.1 ± 0.1	6.9 ± 0.1	3.0 ± 0.1	−10.3 ± 0.1	17 ± 1	0.48 ± 0.04	4	1.0
	0.134 ± 0.003	5.5 ± 0.2	−6.2 ± 0.1	25.2 ± 0.6	6.0 ± 0.1	−5.5 ± 0.1	196 ± 5	2.81 ± 0.13	2	
	0.084 ± 0.003	1.5 ± 0.1	−5.0 ± 0.1	…	…	…	…	…	…	
	0.007 ± 0.003	0.7 ± 0.3	24.4 ± 0.1	…	…	…	…	…	…	
3C018B	0.524 ± 0.006	2.4 ± 0.1	−9.0 ± 0.1	6.6 ± 0.9	2.7 ± 0.3	−10.3 ± 0.3	16 ± 2	0.41 ± 0.06	2	1.0
	0.149 ± 0.005	6.2 ± 0.1	−6.8 ± 0.1	22.5 ± 0.5	7.0 ± 0.1	−6.7 ± 0.1	162 ± 4	2.89 ± 0.10	1	
3C041A	0.033 ± 0.004	8.9 ± 0.2	−1.4 ± 0.1	11.4 ± 0.2	9.5 ± 0.1	−1.4 ± 0.1	351 ± 7	1.99 ± 0.07	3	1.0
	0.011 ± 0.004	1.2 ± 0.2	1.8 ± 0.1	1.0 ± 0.2	1.3 ± 0.1	1.8 ± 0.1	98 ± 16	0.02 ± 0.01	3	
	0.029 ± 0.003	1.7 ± 0.1	−30.5 ± 0.1	…	…	…	…	…	…	
3C041B	0.022 ± 0.005	1.7 ± 0.2	−10.5 ± 0.1	0.3 ± 0.0	1.8 ± 0.1	−10.5 ± 0.1	14 ± 3	0.01 ± 0.00	3	0.5
	0.042 ± 0.006	7.1 ± 0.2	−1.3 ± 0.1	6.2 ± 0.2	7.9 ± 0.1	−1.3 ± 0.1	150 ± 5	0.87 ± 0.05	3	
	0.023 ± 0.005	0.8 ± 0.1	−8.0 ± 0.1	…	…	…	…	…	…	
3C48	0.004 ± 0.001	0.7 ± 0.1	−55.1 ± 0.1	0.1 ± 0.0	0.7 ± 0.1	−52.8 ± 0.1	25 ± 3	0.00 ± 0.00	6	0.5
	0.008 ± 0.001	5.4 ± 0.3	−15.6 ± 0.1	3.1 ± 0.1	6.0 ± 0.1	−15.6 ± 0.1	406 ± 11	0.32 ± 0.02	6	
	0.016 ± 0.001	2.8 ± 0.1	−11.0 ± 0.1	1.3 ± 0.0	3.1 ± 0.1	−11.6 ± 0.1	79 ± 2	0.07 ± 0.00	6	
	0.004 ± 0.001	1.3 ± 0.2	−5.0 ± 0.1	0.6 ± 0.1	1.4 ± 0.1	−5.0 ± 0.1	169 ± 21	0.02 ± 0.00	6	
	0.020 ± 0.001	9.1 ± 0.1	−2.1 ± 0.1	6.7 ± 0.1	10.1 ± 0.1	−2.1 ± 0.1	346 ± 3	1.20 ± 0.02	6	
	0.040 ± 0.001	2.3 ± 0.1	2.6 ± 0.1	1.5 ± 0.0	2.3 ± 0.1	2.8 ± 0.1	38 ± 2	0.07 ± 0.00	6	
4C15.05	0.005 ± 0.001	1.7 ± 0.2	−13.9 ± 0.1	0.4 ± 0.0	1.9 ± 0.1	−13.6 ± 0.1	82 ± 24	0.01 ± 0.00	6	0.0
	0.057 ± 0.001	2.6 ± 0.1	−10.5 ± 0.1	2.4 ± 0.0	2.8 ± 0.1	−11.3 ± 0.1	46 ± 3	0.13 ± 0.01	2	
	0.037 ± 0.001	9.9 ± 0.1	−7.3 ± 0.1	15.9 ± 0.4	10.9 ± 0.1	−7.3 ± 0.1	438 ± 12	3.11 ± 0.13	1	
	0.048 ± 0.001	2.7 ± 0.1	−5.4 ± 0.1	2.6 ± 0.0	2.7 ± 0.1	−5.3 ± 0.1	59 ± 6	0.15 ± 0.02	6	
	0.014 ± 0.001	2.6 ± 0.1	0.3 ± 0.1	2.1 ± 0.1	2.8 ± 0.1	0.3 ± 0.1	145 ± 5	0.10 ± 0.01	6	
	0.001 ± 0.001	5.0 ± 1.1	6.7 ± 0.5	1.5 ± 0.3	5.5 ± 0.1	6.7 ± 0.1	1551 ± 298	0.14 ± 0.05	6	
3C78	0.147 ± 0.004	3.1 ± 0.1	−7.8 ± 0.1	8.7 ± 0.1	3.1 ± 0.1	−7.8 ± 0.1	65 ± 3	0.57 ± 0.03	6	1.0
	0.029 ± 0.004	14.9 ± 0.6	−7.5 ± 0.2	10.8 ± 0.5	15.6 ± 0.1	−7.5 ± 0.1	385 ± 18	3.17 ± 0.25	6	
	0.196 ± 0.004	1.9 ± 0.1	4.2 ± 0.1	7.2 ± 0.1	2.1 ± 0.1	4.0 ± 0.1	39 ± 1	0.29 ± 0.01	1	
	1.369 ± 0.006	2.2 ± 0.1	6.9 ± 0.1	24.1 ± 0.1	2.4 ± 0.1	7.0 ± 0.1	39 ± 7	2.32 ± 0.43	2	
	0.089 ± 0.005	4.1 ± 0.1	11.1 ± 0.1	14.6 ± 0.8	4.6 ± 0.1	11.4 ± 0.1	175 ± 10	1.25 ± 0.11	6	
	0.054 ± 0.006	1.3 ± 0.1	10.4 ± 0.1	…	…	…	…	…	…	
4C16.09	0.014 ± 0.001	1.3 ± 0.1	−9.7 ± 0.1	0.3 ± 0.0	1.6 ± 0.1	−11.7 ± 0.1	25 ± 4	0.01 ± 0.00	6	1.0
	0.436 ± 0.002	4.2 ± 0.1	−1.0 ± 0.1	35.6 ± 0.2	4.1 ± 0.1	−1.0 ± 0.1	106 ± 3	3.74 ± 0.13	6	
	0.227 ± 0.004	1.8 ± 0.1	0.8 ± 0.1	6.5 ± 0.2	1.8 ± 0.1	0.9 ± 0.1	54 ± 10	0.44 ± 0.08	6	
	0.086 ± 0.001	5.4 ± 0.1	5.9 ± 0.1	21.4 ± 0.2	5.9 ± 0.1	5.7 ± 0.1	260 ± 3	2.37 ± 0.05	6	
	0.042 ± 0.001	1.8 ± 0.1	7.6 ± 0.1	4.4 ± 0.2	1.9 ± 0.1	7.5 ± 0.1	120 ± 8	0.17 ± 0.01	6	
	0.013 ± 0.001	4.1 ± 0.2	−8.7 ± 0.1	…	…	…	…	…	…	
3C111A	0.013 ± 0.003	5.7 ± 1.0	−28.9 ± 0.4	6.3 ± 0.5	6.2 ± 0.1	−27.0 ± 0.1	487 ± 44	0.69 ± 0.15	3	1.0
	0.041 ± 0.003	2.6 ± 0.1	−21.9 ± 0.1	5.4 ± 0.2	2.8 ± 0.1	−20.5 ± 0.1	131 ± 6	0.27 ± 0.02	1	
	0.322 ± 0.004	2.6 ± 0.1	−16.8 ± 0.1	8.5 ± 0.1	2.9 ± 0.1	−16.6 ± 0.1	34 ± 5	0.56 ± 0.10	5	
	0.172 ± 0.005	8.6 ± 0.3	−9.1 ± 0.2	40.7 ± 1.3	9.5 ± 0.1	−9.0 ± 0.1	248 ± 10	7.18 ± 0.47	12	
	0.201 ± 0.011	1.5 ± 0.1	−4.7 ± 0.1	12.2 ± 0.7	1.6 ± 0.1	−4.6 ± 0.1	65 ± 15	0.38 ± 0.10	2	
	0.790 ± 0.009	3.9 ± 0.1	−1.8 ± 0.1	39.3 ± 0.7	4.1 ± 0.1	−1.6 ± 0.1	77 ± 4	4.57 ± 0.32	4	
	0.643 ± 0.020	3.3 ± 0.1	1.8 ± 0.1	41.0 ± 1.9	3.6 ± 0.1	1.8 ± 0.1	93 ± 8	3.85 ± 0.38	12	
	0.232 ± 0.004	5.2 ± 0.1	6.1 ± 0.1	26.8 ± 0.4	5.7 ± 0.1	6.0 ± 0.1	129 ± 1	3.02 ± 0.10	12	
	0.037 ± 0.003	1.7 ± 0.1	−32.4 ± 0.1	…	…	…	…	…	…	
	0.025 ± 20000.0	0.1 ± 10000.0	6.6 ± 900.0	…	…	…	…	…	…	
	0.114 ± 0.006	2.1 ± 0.1	−8.3 ± 0.1	…	…	…	…	…	…	
	0.069 ± 0.004	1.3 ± 0.1	8.4 ± 0.1	…	…	…	…	…	…	
3C111B	0.019 ± 0.002	1.7 ± 0.1	−54.8 ± 0.1	0.5 ± 0.0	1.7 ± 0.1	−56.2 ± 0.1	26 ± 1	0.02 ± 0.00	10	1.0
	0.111 ± 0.003	2.7 ± 0.1	−16.8 ± 0.1	2.8 ± 0.1	3.0 ± 0.1	−16.7 ± 0.1	30 ± 5	0.17 ± 0.03	1	
	0.092 ± 0.004	12.1 ± 0.3	−10.8 ± 0.3	35.9 ± 1.0	12.7 ± 0.1	−10.8 ± 0.1	409 ± 10	8.86 ± 0.42	10	
	0.400 ± 0.005	2.8 ± 0.1	−8.3 ± 0.1	3.7 ± 0.1	3.1 ± 0.1	−8.3 ± 0.1	14 ± 8	0.32 ± 0.20	10	
	0.967 ± 0.020	3.7 ± 0.1	−1.7 ± 0.1	29.2 ± 1.1	3.9 ± 0.1	−1.7 ± 0.1	56 ± 5	3.88 ± 0.43	10	

Table 5
(Continued)

Source (name)	τ_0	Δv_0 (km s^{-1})	v_0 (km s^{-1})	$T_{B,n}$ (K)	$\Delta v_{0,n}$ (km s^{-1})	$v_{0,n}$ (km s^{-1})	T_s (K)	$N(\mathrm{H\,I})_{\mathrm{abs}_2}$ (10^{20} cm^{-2})	$\mathcal{O}$	$\mathcal{F}$
	0.347 ± 0.054	2.7 ± 0.1	2.1 ± 0.1	11.1 ± 3.1	2.7 ± 0.1	2.1 ± 0.1	58 ± 13	1.07 ± 0.31	2	
	0.342 ± 0.032	5.6 ± 0.4	3.7 ± 0.4	33.8 ± 3.8	6.2 ± 0.1	3.9 ± 0.1	120 ± 12	4.51 ± 0.71	10	
	0.181 ± 0.006	0.8 ± 0.1	−2.3 ± 0.1	…	…	…	…	…	…	
	0.015 ± 0.002	2.2 ± 0.2	−51.3 ± 0.1	…	…	…	…	…	…	
	0.212 ± 0.005	2.1 ± 0.1	8.0 ± 0.1	…	…	…	…	…	…	
3C111C	0.027 ± 0.004	2.4 ± 0.2	−31.4 ± 0.1	0.9 ± 0.1	2.6 ± 0.1	−31.4 ± 0.1	35 ± 3	0.04 ± 0.01	11	1.0
	0.029 ± 0.004	2.6 ± 0.2	−27.8 ± 0.1	1.1 ± 0.1	2.9 ± 0.1	−26.0 ± 0.1	39 ± 2	0.06 ± 0.01	11	
	0.282 ± 0.045	2.1 ± 0.1	−16.9 ± 0.1	3.9 ± 0.9	2.1 ± 0.1	−17.8 ± 0.1	20 ± 4	0.23 ± 0.07	11	
	0.088 ± 0.027	2.5 ± 0.6	−15.3 ± 0.5	8.4 ± 2.4	2.8 ± 0.1	−14.1 ± 0.1	90 ± 34	0.39 ± 0.22	1	
	0.182 ± 0.011	11.2 ± 0.6	−8.1 ± 0.6	17.8 ± 1.3	12.4 ± 0.1	−8.1 ± 0.1	118 ± 28	4.69 ± 1.20	11	
	0.816 ± 0.050	2.3 ± 0.1	−2.1 ± 0.1	3.5 ± 1.0	2.3 ± 0.1	−2.4 ± 0.1	20 ± 11	0.75 ± 0.44	11	
	0.456 ± 0.044	7.3 ± 0.3	1.6 ± 0.4	34.6 ± 4.7	8.1 ± 0.1	1.6 ± 0.1	108 ± 18	7.00 ± 1.41	11	
	0.584 ± 0.043	2.5 ± 0.1	1.1 ± 0.1	…	…	…	…	…	…	
	0.416 ± 0.008	1.6 ± 0.1	−8.4 ± 0.1	…	…	…	…	…	…	
	0.211 ± 0.014	1.5 ± 0.1	−5.5 ± 0.1	…	…	…	…	…	…	
	0.058 ± 0.007	1.8 ± 0.2	6.3 ± 0.1	…	…	…	…	…	…	
3C120	0.617 ± 0.005	1.3 ± 0.1	6.1 ± 0.1	7.7 ± 0.1	1.3 ± 0.1	5.5 ± 0.1	20 ± 9	0.31 ± 0.15	2	1.0
	1.681 ± 0.004	4.4 ± 0.1	7.3 ± 0.1	36.6 ± 0.2	4.9 ± 0.1	6.6 ± 0.1	44 ± 4	6.35 ± 0.60	1	
	0.776 ± 0.012	2.3 ± 0.1	9.9 ± 0.1	12.7 ± 0.3	2.5 ± 0.1	10.6 ± 0.1	23 ± 5	0.82 ± 0.18	3	
3C123A	0.064 ± 0.001	3.1 ± 0.1	−19.9 ± 0.1	1.5 ± 0.0	3.8 ± 0.1	−21.1 ± 0.1	26 ± 2	0.10 ± 0.01	7	1.0
	0.379 ± 0.035	2.2 ± 0.1	1.6 ± 0.1	3.2 ± 0.7	2.2 ± 0.1	1.9 ± 0.1	19 ± 14	0.32 ± 0.23	7	
	0.044 ± 0.004	10.1 ± 0.3	3.7 ± 0.1	27.0 ± 2.8	12.2 ± 0.1	3.9 ± 0.1	619 ± 79	5.36 ± 0.91	7	
	0.810 ± 0.071	4.4 ± 0.1	5.3 ± 0.2	23.1 ± 4.6	5.3 ± 0.1	5.2 ± 0.1	67 ± 25	4.67 ± 1.86	7	
	0.628 ± 0.037	1.8 ± 0.1	5.5 ± 0.1	4.3 ± 0.7	1.7 ± 0.1	6.3 ± 0.1	18 ± 11	0.40 ± 0.25	7	
	0.008 ± 0.001	4.0 ± 0.3	20.2 ± 0.1	1.0 ± 0.1	4.0 ± 0.1	17.9 ± 0.1	124 ± 9	0.08 ± 0.01	7	
	1.020 ± 0.096	2.3 ± 0.1	3.7 ± 0.1	…	…	…	…	…	…	
3C123B	0.064 ± 0.001	3.2 ± 0.1	−19.3 ± 0.1	0.9 ± 0.0	3.6 ± 0.1	−20.4 ± 0.1	16 ± 2	0.07 ± 0.01	6	1.0
	1.648 ± 0.005	4.3 ± 0.1	4.4 ± 0.1	17.6 ± 0.2	4.8 ± 0.1	4.4 ± 0.1	36 ± 14	5.08 ± 1.98	3	
	0.042 ± 0.003	10.9 ± 0.3	4.9 ± 0.1	27.8 ± 2.2	10.9 ± 0.1	4.5 ± 0.1	664 ± 52	5.98 ± 0.71	2	
	0.253 ± 0.007	1.5 ± 0.1	5.5 ± 0.1	5.4 ± 0.6	1.6 ± 0.1	6.0 ± 0.1	81 ± 43	0.59 ± 0.32	6	
	0.004 ± 0.001	3.2 ± 0.5	20.1 ± 0.2	1.4 ± 0.2	3.5 ± 0.1	18.3 ± 0.1	334 ± 52	0.09 ± 0.02	1	
	0.064 ± 0.003	1.7 ± 0.1	8.5 ± 0.1	…	…	…	…	…	…	
3C132	0.197 ± 0.009	7.2 ± 0.1	1.7 ± 0.1	27.8 ± 1.5	7.2 ± 0.1	1.9 ± 0.1	165 ± 12	4.57 ± 0.41	7	1.0
	1.472 ± 0.005	2.0 ± 0.1	7.8 ± 0.9	7.1 ± 0.1	2.0 ± 0.1	7.8 ± 0.1	27 ± 19	1.55 ± 1.12	4	
	0.230 ± 0.003	6.7 ± 0.1	12.1 ± 0.1	16.2 ± 0.1	7.3 ± 0.1	11.4 ± 0.1	80 ± 4	2.39 ± 0.15	3	
	0.129 ± 0.022	1.8 ± 0.1	1.7 ± 99.	…	…	…	…	…	…	
	0.273 ± 0.010	1.5 ± 0.1	9.4 ± 0.1	…	…	…	…	…	…	
	0.059 ± 0.004	2.4 ± 0.1	14.8 ± 0.1	…	…	…	…	…	…	
	0.042 ± 0.017	3.4 ± 0.1	2.2 ± 0.1	…	…	…	…	…	…	
3C133	0.033 ± 0.005	9.5 ± 0.3	−29.8 ± 0.1	17.2 ± 0.9	10.4 ± 0.1	−28.8 ± 0.1	537 ± 28	3.26 ± 0.26	8	1.0
	0.134 ± 0.007	2.4 ± 0.1	−1.5 ± 0.1	2.1 ± 0.1	2.7 ± 0.1	−1.6 ± 0.1	26 ± 16	0.17 ± 0.11	2	
	0.240 ± 0.011	9.6 ± 0.1	3.1 ± 0.1	59.2 ± 3.0	9.6 ± 0.1	2.8 ± 0.1	283 ± 13	12.67 ± 0.87	1	
	0.706 ± 0.010	2.7 ± 0.1	3.7 ± 0.1	2.7 ± 0.1	3.0 ± 0.1	3.4 ± 0.1	11 ± 15	0.44 ± 0.61	8	
	0.845 ± 0.029	1.5 ± 0.1	7.6 ± 0.1	1.6 ± 0.7	1.5 ± 0.1	7.6 ± 0.1	23 ± 19	0.58 ± 0.48	8	
	0.780 ± 0.022	2.6 ± 0.1	8.4 ± 0.1	18.0 ± 1.0	2.9 ± 0.1	8.7 ± 0.1	46 ± 9	1.82 ± 0.37	8	
	0.084 ± 0.005	3.2 ± 0.1	−27.8 ± 0.1	…	…	…	…	…	…	
	0.077 ± 0.005	1.6 ± 0.1	−4.2 ± 0.1	…	…	…	…	…	…	
3C138	0.033 ± 0.001	2.3 ± 0.1	−22.0 ± 0.1	1.9 ± 0.1	2.5 ± 0.1	−21.2 ± 0.1	60 ± 2	0.09 ± 0.01	8	1.0
	0.026 ± 0.002	4.3 ± 0.2	−6.7 ± 0.1	7.7 ± 0.3	4.5 ± 0.1	−6.7 ± 0.1	297 ± 11	0.65 ± 0.05	8	
	0.322 ± 0.003	4.3 ± 0.1	0.0 ± 0.1	33.4 ± 0.2	4.8 ± 0.1	0.0 ± 0.1	125 ± 3	3.39 ± 0.09	8	
	0.079 ± 0.003	1.2 ± 0.1	1.6 ± 0.1	2.0 ± 0.2	1.3 ± 0.1	1.6 ± 0.1	47 ± 19	0.08 ± 0.04	8	
	0.003 ± 0.003	37.4 ± 4.9	2.9 ± 1.5	4.8 ± 1.1	33.7 ± 0.1	2.6 ± 0.1	1427 ± 302	3.52 ± 1.23	8	
	1.057 ± 0.005	2.4 ± 0.1	6.3 ± 0.1	20.6 ± 0.2	2.6 ± 0.1	5.9 ± 0.1	39 ± 7	1.92 ± 0.38	8	
	0.432 ± 0.003	3.0 ± 0.1	9.0 ± 0.1	23.5 ± 0.2	3.3 ± 0.1	9.5 ± 0.1	66 ± 1	1.68 ± 0.04	8	
	0.011 ± 0.002	2.7 ± 0.5	13.3 ± 0.2	4.2 ± 0.5	3.0 ± 0.1	12.0 ± 0.1	422 ± 55	0.24 ± 0.06	8	
PKS0531	0.001 ± 0.001	12.1 ± 1.5	−24.3 ± 0.5	2.9 ± 0.5	13.3 ± 0.1	−24.3 ± 0.1	2049 ± 400	0.68 ± 0.20	10	1.0
	0.007 ± 0.001	3.5 ± 0.2	−23.0 ± 0.1	0.1 ± 0.0	3.8 ± 0.1	−20.7 ± 0.1	24 ± 4	0.01 ± 0.00	10	
	0.006 ± 0.001	6.2 ± 0.3	−9.0 ± 0.1	0.8 ± 0.0	6.8 ± 0.1	−9.0 ± 0.1	240 ± 130	0.16 ± 0.09	1	

Table 5
(Continued)

Source (name)	τ_0	Δv_0 (km s^{-1})	v_0 (km s^{-1})	$T_{B,n}$ (K)	$\Delta v_{0,n}$ (km s^{-1})	$v_{0,n}$ (km s^{-1})	T_s (K)	$N(\mathrm{H\,I})_{\mathrm{abs}_2}$ (10^{20} cm^{-2})	$\mathcal{O}$	$\mathcal{F}$
	0.403 ± 0.009	1.9 ± 0.1	1.6 ± 0.1	3.7 ± 0.3	1.9 ± 0.1	1.5 ± 0.1	28 ± 26	0.44 ± 0.40	3	
	0.141 ± 0.005	9.7 ± 0.1	4.6 ± 0.1	69.4 ± 2.7	10.3 ± 0.1	4.3 ± 0.1	542 ± 25	14.48 ± 0.89	2	
	0.190 ± 0.003	2.4 ± 0.1	9.5 ± 0.1	14.9 ± 0.3	2.6 ± 0.1	10.0 ± 0.1	100 ± 10	0.88 ± 0.09	10	
	0.019 ± 0.001	2.3 ± 0.2	12.1 ± 0.1	3.0 ± 0.2	2.5 ± 0.1	12.1 ± 0.1	132 ± 31	0.11 ± 0.03	10	
	0.005 ± 0.001	4.1 ± 0.2	21.0 ± 0.1	2.0 ± 0.1	4.5 ± 0.1	20.9 ± 0.1	380 ± 14	0.16 ± 0.01	10	
	0.075 ± 0.005	2.7 ± 0.1	6.0 ± 0.1	…	…	…	…	…	…	
	0.088 ± 0.007	1.9 ± 0.1	3.2 ± 0.1	…	…	…	…	…	…	
3C147	0.013 ± 0.001	2.0 ± 0.1	−19.4 ± 0.1	0.8 ± 0.0	2.2 ± 0.1	−19.4 ± 0.1	65 ± 5	0.03 ± 0.00	9	1.0
	0.054 ± 0.009	1.9 ± 0.1	−13.7 ± 0.1	2.0 ± 0.3	2.0 ± 0.1	−15.0 ± 0.1	36 ± 8	0.07 ± 0.02	9	
	0.120 ± 0.021	6.4 ± 0.3	−11.1 ± 0.1	23.9 ± 4.5	6.6 ± 0.1	−11.2 ± 0.1	218 ± 37	3.25 ± 0.82	9	
	0.165 ± 0.020	2.3 ± 0.1	−10.7 ± 0.1	5.0 ± 0.7	2.1 ± 0.1	−9.9 ± 0.1	37 ± 6	0.27 ± 0.06	9	
	0.278 ± 0.004	5.9 ± 0.1	0.5 ± 0.1	23.6 ± 0.4	6.5 ± 0.1	0.6 ± 0.1	109 ± 9	3.49 ± 0.33	9	
	0.035 ± 0.001	1.6 ± 0.1	5.1 ± 0.1	0.9 ± 0.0	1.8 ± 0.1	5.6 ± 0.1	25 ± 3	0.03 ± 0.00	9	
	0.725 ± 0.006	1.7 ± 0.1	−8.0 ± 0.1	…	…	…	…	…	…	
	0.208 ± 0.004	2.0 ± 0.1	−0.1 ± 0.1	…	…	…	…	…	…	
	0.042 ± 0.003	1.5 ± 0.1	1.8 ± 0.1	…	…	…	…	…	…	
3C154	0.061 ± 0.005	3.1 ± 0.2	−23.2 ± 0.1	1.6 ± 0.1	3.4 ± 0.1	−23.1 ± 0.1	25 ± 3	0.10 ± 0.02	5	1.0
	0.012 ± 0.005	7.4 ± 1.4	−22.9 ± 0.3	7.2 ± 3.0	7.4 ± 0.1	−22.4 ± 0.1	587 ± 240	1.05 ± 0.65	6	
	0.123 ± 0.020	14.0 ± 0.5	0.6 ± 0.2	87.5 ± 14.8	15.0 ± 0.1	0.7 ± 0.1	762 ± 130	25.55 ± 6.15	2	
	1.300 ± 0.015	2.3 ± 0.1	2.0 ± 0.1	4.2 ± 0.2	2.2 ± 0.1	2.0 ± 0.1	10 ± 15	0.62 ± 0.91	4	
	0.733 ± 0.016	3.9 ± 0.1	4.8 ± 0.1	7.0 ± 0.3	3.9 ± 0.1	4.8 ± 0.1	19 ± 17	1.11 ± 0.99	1	
	0.521 ± 0.004	2.2 ± 0.1	10.8 ± 0.1	7.0 ± 0.1	2.5 ± 0.1	11.8 ± 0.1	19 ± 3	0.44 ± 0.08	3	
	0.297 ± 0.008	1.1 ± 0.1	−2.2 ± 0.1	…	…	…	…	…	…	
	0.975 ± 0.015	4.6 ± 0.1	−2.6 ± 0.1	…	…	…	…	…	…	
PKS0742	0.009 ± 0.001	3.2 ± 0.1	1.5 ± 0.1	1.5 ± 0.1	3.5 ± 0.2	1.6 ± 0.1	164 ± 9	0.09 ± 0.01	1	0.0
3C225A	0.043 ± 0.002	1.8 ± 0.1	−40.2 ± 0.1	0.9 ± 0.0	1.9 ± 0.1	−39.6 ± 0.1	22 ± 0	0.03 ± 0.00	5	1.0
	0.020 ± 0.002	4.8 ± 0.3	−37.4 ± 0.2	1.2 ± 0.0	4.7 ± 0.1	−38.3 ± 0.1	60 ± 1	0.11 ± 0.01	5	
	0.048 ± 0.002	2.5 ± 0.1	−27.2 ± 0.1	1.0 ± 0.0	2.8 ± 0.1	−27.7 ± 0.1	22 ± 0	0.05 ± 0.00	5	
	0.013 ± 0.002	7.7 ± 0.3	−5.2 ± 0.1	4.3 ± 0.1	8.1 ± 0.1	−4.9 ± 0.1	327 ± 11	0.64 ± 0.04	5	
	0.805 ± 0.002	1.3 ± 0.1	4.0 ± 0.1	5.7 ± 0.0	1.4 ± 0.1	3.6 ± 0.1	11 ± 2	0.23 ± 0.04	5	
3C225B	0.044 ± 0.003	2.0 ± 0.1	−40.3 ± 0.1	0.8 ± 0.0	1.9 ± 0.1	−39.8 ± 0.1	18 ± 0	0.03 ± 0.00	5	1.0
	0.023 ± 0.003	4.0 ± 0.3	−37.2 ± 0.1	3.3 ± 0.1	4.0 ± 0.1	−37.4 ± 0.1	145 ± 4	0.26 ± 0.02	5	
	0.053 ± 0.003	2.4 ± 0.1	−27.3 ± 0.1	1.0 ± 0.0	2.9 ± 0.1	−27.8 ± 0.1	20 ± 0	0.05 ± 0.00	5	
	0.013 ± 0.003	8.3 ± 0.4	−5.6 ± 0.2	6.1 ± 0.2	8.3 ± 0.1	−4.5 ± 0.1	458 ± 17	1.00 ± 0.07	5	
	0.774 ± 0.003	1.3 ± 0.1	4.0 ± 0.1	7.7 ± 0.0	1.5 ± 0.1	3.5 ± 0.1	14 ± 0	0.28 ± 0.01	5	
3C236	…	…	…	…	…	…	…	…	…	
3C237	0.006 ± 0.001	15.0 ± 0.6	−4.0 ± 0.3	2.1 ± 0.1	14.8 ± 0.1	−4.0 ± 0.1	382 ± 17	0.63 ± 0.05	3	1.0
	0.415 ± 0.001	1.2 ± 0.1	2.3 ± 0.1	4.3 ± 0.0	1.2 ± 0.1	2.1 ± 0.1	13 ± 0	0.13 ± 0.00	3	
	0.005 ± 0.001	1.9 ± 0.2	−2.4 ± 0.1	…	…	…	…	…	…	
3C245A	0.010 ± 0.002	5.3 ± 0.3	−9.1 ± 0.1	3.9 ± 0.3	5.3 ± 0.1	−8.8 ± 0.1	385 ± 30	0.40 ± 0.05	2	0.5
	0.006 ± 0.002	1.6 ± 0.3	−9.8 ± 0.1	…	…	…	…	…	…	
3C245B	…	…	…	…	…	…	…	…	…	
1055+018	0.006 ± 0.001	7.1 ± 0.3	−7.3 ± 0.1	6.0 ± 0.2	7.0 ± 0.1	−6.8 ± 0.1	941 ± 30	0.83 ± 0.05	1	1.0
3C263.1	0.007 ± 0.001	1.3 ± 0.1	−68.9 ± 0.1	0.1 ± 0.0	1.4 ± 0.1	−65.4 ± 0.1	15 ± 1	0.00 ± 0.00	3	1.0
	0.020 ± 0.001	2.0 ± 0.1	−52.8 ± 0.1	0.7 ± 0.0	2.1 ± 0.1	−54.3 ± 0.1	35 ± 0	0.03 ± 0.00	3	
	0.007 ± 0.001	0.6 ± 0.1	15.6 ± 0.1	0.3 ± 0.0	0.6 ± 0.1	16.9 ± 0.1	42 ± 5	0.00 ± 0.00	3	
3C273	0.019 ± 0.001	2.3 ± 0.1	−6.3 ± 0.1	0.3 ± 0.0	2.5 ± 0.1	−5.7 ± 0.1	17 ± 0	0.02 ± 0.00	3	1.0
	0.005 ± 0.001	6.4 ± 0.3	−5.8 ± 0.1	2.4 ± 0.2	7.0 ± 0.1	−5.7 ± 0.1	455 ± 47	0.29 ± 0.04	3	
	0.003 ± 0.001	2.0 ± 0.2	31.6 ± 0.1	…	…	…	…	…	…	
4C32.44	0.018 ± 0.001	2.8 ± 0.1	−16.2 ± 0.1	2.0 ± 0.0	3.1 ± 0.1	−16.5 ± 0.1	112 ± 2	0.11 ± 0.00	2	1.0
	0.004 ± 0.001	3.7 ± 0.3	−4.2 ± 0.1	0.9 ± 0.1	3.9 ± 0.1	−4.6 ± 0.1	255 ± 17	0.07 ± 0.01	2	
4C25.43	…	…	…	…	…	…	…	…	…	

Table 5
(Continued)

Source (name)	τ_0	Δv_0 (km s^{-1})	v_0 (km s^{-1})	$T_{B,n}$ (K)	$\Delta v_{0,n}$ (km s^{-1})	$v_{0,n}$ (km s^{-1})	T_s (K)	$N(\mathrm{H\,I})_{\mathrm{abs}_2}$ (10^{20} cm^{-2})	$\mathscr{O}$	$\mathscr{F}$
3C286	0.006 ± 0.001	2.4 ± 0.1	−28.5 ± 0.1	0.5 ± 0.0	2.6 ± 0.1	−28.8 ± 0.1	76 ± 2	0.02 ± 0.00	3	0.0
	0.005 ± 0.001	3.2 ± 0.2	−14.2 ± 0.1	0.3 ± 0.0	3.5 ± 0.1	−13.6 ± 0.1	60 ± 2	0.02 ± 0.00	3	
	0.007 ± 0.001	4.3 ± 0.1	−7.3 ± 0.1	0.6 ± 0.0	4.8 ± 0.1	−6.6 ± 0.1	78 ± 2	0.05 ± 0.00	3	
4C12.50	0.016 ± 0.001	6.6 ± 0.1	−2.5 ± 0.1	5.1 ± 0.2	6.5 ± 0.1	−2.5 ± 0.1	318 ± 11	0.66 ± 0.04	2	1.0
	0.077 ± 0.002	2.2 ± 0.1	−1.0 ± 0.1	7.2 ± 0.1	2.4 ± 0.1	−1.0 ± 0.1	97 ± 1	0.33 ± 0.01	1	
3C298	0.019 ± 0.001	3.6 ± 0.1	−1.1 ± 0.1	2.1 ± 0.2	4.3 ± 0.4	−1.1 ± 0.2	112 ± 10	0.15 ± 0.01	1	0.5
UGC09799	0.058 ± 0.010	2.7 ± 0.1	−4.2 ± 0.1	3.1 ± 0.2	2.9 ± 0.1	−4.2 ± 0.1	58 ± 4	0.17 ± 0.02	1	1.0
4C04.51	0.002 ± 0.001	14.0 ± 1.5	−9.2 ± 0.8	0.3 ± 0.0	15.5 ± 0.1	−9.1 ± 0.1	114 ± 8	0.07 ± 0.01	3	0.0
	0.025 ± 0.001	2.4 ± 0.1	−4.0 ± 0.1	5.2 ± 0.1	2.4 ± 0.1	−4.0 ± 0.1	207 ± 5	0.24 ± 0.01	3	
	0.067 ± 0.001	3.4 ± 0.1	−0.6 ± 0.1	12.1 ± 0.1	3.8 ± 0.1	−0.6 ± 0.1	183 ± 2	0.82 ± 0.02	3	
3C327.1A	0.126 ± 0.006	3.4 ± 0.1	−2.7 ± 0.1	16.3 ± 0.3	3.7 ± 0.1	−2.9 ± 0.1	140 ± 3	1.16 ± 0.06	1	1.0
	0.425 ± 0.010	1.9 ± 0.1	−0.0 ± 0.1	19.8 ± 0.6	2.0 ± 0.1	−0.0 ± 0.1	63 ± 4	1.00 ± 0.08	2	
	0.401 ± 0.008	2.2 ± 0.1	2.0 ± 0.1	22.2 ± 0.4	2.4 ± 0.1	2.0 ± 0.1	69 ± 3	1.18 ± 0.06	3	
3C327.1B	0.118 ± 0.006	3.2 ± 0.1	−2.7 ± 0.1	15.6 ± 0.3	3.6 ± 0.1	−3.0 ± 0.1	142 ± 3	1.05 ± 0.06	4	1.0
	0.359 ± 0.011	1.9 ± 0.1	−0.0 ± 0.1	20.3 ± 0.8	2.1 ± 0.1	−0.0 ± 0.1	74 ± 4	1.01 ± 0.08	4	
	0.419 ± 0.008	2.2 ± 0.1	1.9 ± 0.1	22.2 ± 0.6	2.4 ± 0.1	1.9 ± 0.1	68 ± 3	1.20 ± 0.07	4	
	0.013 ± 0.003	0.7 ± 0.1	46.1 ± 0.1	…	…	…	…	…	…	
PKS1607	0.128 ± 0.001	2.0 ± 0.1	−10.3 ± 0.1	3.0 ± 0.0	2.0 ± 0.1	−10.7 ± 0.1	26 ± 1	0.13 ± 0.01	1	1.0
	0.013 ± 0.001	6.5 ± 0.3	−7.8 ± 0.2	1.4 ± 0.0	7.2 ± 0.1	−7.8 ± 0.1	114 ± 10	0.19 ± 0.02	2	
	0.064 ± 0.004	3.9 ± 0.1	−1.2 ± 0.1	7.0 ± 0.4	4.3 ± 0.1	−1.1 ± 0.1	115 ± 10	0.56 ± 0.06	4	
	0.123 ± 0.004	2.2 ± 0.1	−2.3 ± 0.1	…	…	…	…	…	…	
J1613	…	…	…	…	…	…	…	…	…	
3C345	0.009 ± 0.001	0.6 ± 0.1	−5.2 ± 0.1	…	…	…	…	…	…	0.0
3C346	0.035 ± 0.003	4.5 ± 0.1	−6.4 ± 0.1	4.5 ± 0.1	4.9 ± 0.1	−6.4 ± 0.1	133 ± 3	0.40 ± 0.02	3	1.0
	0.279 ± 0.004	2.0 ± 0.1	−0.6 ± 0.1	13.2 ± 0.1	2.1 ± 0.1	−0.6 ± 0.1	58 ± 4	0.62 ± 0.04	3	
	0.197 ± 0.004	1.9 ± 0.1	2.1 ± 0.1	9.8 ± 0.1	2.1 ± 0.1	2.1 ± 0.1	59 ± 4	0.43 ± 0.03	3	
3C390	0.103 ± 0.006	2.2 ± 0.1	1.0 ± 0.1	14.6 ± 0.8	2.5 ± 0.1	0.9 ± 0.1	143 ± 11	0.64 ± 0.06	10	0.5
	0.146 ± 0.003	3.7 ± 0.2	3.7 ± 0.1	30.5 ± 0.6	4.0 ± 0.1	3.4 ± 0.1	221 ± 7	2.31 ± 0.14	3	
	0.082 ± 0.003	5.7 ± 0.2	8.8 ± 0.2	26.2 ± 0.4	6.3 ± 0.1	8.8 ± 0.1	331 ± 7	3.01 ± 0.13	10	
	0.043 ± 0.003	2.0 ± 0.1	11.2 ± 0.1	1.1 ± 0.1	2.2 ± 0.1	12.3 ± 0.1	27 ± 4	0.05 ± 0.01	10	
	0.095 ± 0.003	9.8 ± 0.1	24.5 ± 0.1	37.7 ± 0.5	10.7 ± 0.1	25.5 ± 0.1	415 ± 6	7.51 ± 0.17	1	
	0.067 ± 0.003	1.4 ± 0.1	28.7 ± 0.1	2.0 ± 0.0	1.5 ± 0.1	30.8 ± 0.1	30 ± 4	0.06 ± 0.01	10	
	0.007 ± 0.002	9.2 ± 1.1	42.2 ± 0.3	18.1 ± 1.1	10.2 ± 0.1	42.1 ± 0.1	2613 ± 177	3.24 ± 0.48	2	
	0.022 ± 0.002	1.7 ± 0.1	35.8 ± 0.1	…	…	…	…	…	…	
	0.033 ± 0.003	2.0 ± 0.1	24.0 ± 0.1	…	…	…	…	…	…	
	0.006 ± 0.002	0.6 ± 0.2	17.1 ± 0.1	…	…	…	…	…	…	
4C33.48	0.170 ± 0.006	2.2 ± 0.1	3.5 ± 0.1	3.6 ± 0.1	2.4 ± 0.1	3.3 ± 0.1	26 ± 5	0.20 ± 0.04	4	1.0
	0.139 ± 0.006	6.8 ± 0.1	25.4 ± 0.1	8.5 ± 0.3	6.8 ± 0.1	23.5 ± 0.1	75 ± 13	1.39 ± 0.25	4	
	0.277 ± 0.006	2.3 ± 0.1	23.8 ± 0.1	…	…	…	…	…	…	
	0.128 ± 0.005	1.7 ± 0.1	28.8 ± 0.1	…	…	…	…	…	…	
3C409A	0.443 ± 0.004	3.2 ± 0.1	4.2 ± 0.1	23.6 ± 0.1	3.5 ± 0.1	4.2 ± 0.1	64 ± 9	1.77 ± 0.27	1	0.5
	0.332 ± 0.005	3.0 ± 0.1	7.9 ± 0.1	34.0 ± 0.2	3.0 ± 0.1	7.9 ± 0.1	122 ± 11	2.36 ± 0.22	2	
	0.732 ± 0.007	2.1 ± 0.1	13.8 ± 0.1	5.8 ± 0.1	2.1 ± 0.1	12.5 ± 0.1	13 ± 5	0.41 ± 0.16	7	
	0.440 ± 0.008	6.5 ± 0.1	14.6 ± 0.1	49.2 ± 1.2	6.8 ± 0.1	14.5 ± 0.1	145 ± 20	8.11 ± 1.18	7	
	0.735 ± 0.006	1.7 ± 0.1	15.9 ± 0.1	0.6 ± 0.1	1.6 ± 0.1	15.9 ± 0.1	12 ± 18	0.29 ± 0.45	7	
	0.020 ± 0.003	4.3 ± 0.2	24.3 ± 0.1	7.1 ± 0.3	4.8 ± 0.1	24.6 ± 0.1	366 ± 39	0.63 ± 0.08	7	
	0.004 ± 0.002	0.6 ± 0.2	−53.8 ± 0.1	…	…	…	…	…	…	
3C409B	0.429 ± 0.003	2.9 ± 0.1	4.0 ± 0.1	14.0 ± 0.1	3.2 ± 0.1	3.6 ± 0.1	49 ± 9	1.18 ± 0.24	1	1.0
	0.280 ± 0.007	3.0 ± 0.1	8.0 ± 0.1	24.9 ± 0.8	3.1 ± 0.1	8.0 ± 0.1	120 ± 13	1.97 ± 0.23	3	
	0.631 ± 0.081	1.9 ± 0.1	13.6 ± 0.1	7.2 ± 5.2	1.8 ± 0.1	13.9 ± 0.1	66 ± 22	1.51 ± 0.55	6	
	0.106 ± 0.004	13.1 ± 0.2	14.5 ± 0.2	28.5 ± 1.1	14.4 ± 0.1	15.9 ± 0.1	285 ± 12	7.67 ± 0.46	6	
	0.890 ± 0.065	3.0 ± 0.1	15.3 ± 0.1	16.7 ± 3.0	3.0 ± 0.1	15.6 ± 0.1	47 ± 13	2.45 ± 0.73	2	
	0.193 ± 0.053	3.6 ± 1.2	12.3 ± 0.9	…	…	…	…	…	…	

Table 5
(Continued)

Source (name)	τ_0	Δv_0 (km s^{-1})	v_0 (km s^{-1})	$T_{B,n}$ (K)	$\Delta v_{0,n}$ (km s^{-1})	$v_{0,n}$ (km s^{-1})	T_s (K)	$N(\mathrm{H\,I})_{\mathrm{abs}_2}$ (10^{20} cm^{-2})	$\mathcal{O}$	$\mathcal{F}$
3C410A	0.014 ± 0.002	1.5 ± 0.1	−30.2 ± 0.1	0.2 ± 0.0	1.5 ± 0.1	−30.2 ± 0.1	15 ± 3	0.01 ± 0.00	13	1.0
	0.020 ± 0.003	4.0 ± 0.2	−22.7 ± 0.1	12.6 ± 0.6	4.0 ± 0.1	−23.4 ± 0.1	647 ± 31	0.99 ± 0.09	13	
	0.613 ± 0.018	3.6 ± 0.1	−0.2 ± 0.1	17.5 ± 0.9	3.9 ± 0.1	−0.2 ± 0.1	48 ± 12	2.07 ± 0.55	13	
	0.648 ± 0.023	3.2 ± 0.1	2.7 ± 0.1	17.9 ± 1.1	3.6 ± 0.1	2.7 ± 0.1	49 ± 14	2.02 ± 0.60	13	
	1.693 ± 0.150	3.2 ± 0.1	7.4 ± 0.1	47.0 ± 9.9	3.5 ± 0.1	6.7 ± 0.1	70 ± 13	7.33 ± 1.64	13	
	1.864 ± 0.125	1.5 ± 0.1	8.1 ± 0.1	11.6 ± 12.2	1.6 ± 0.1	8.1 ± 0.1	104 ± 60	5.79 ± 3.46	13	
	0.149 ± 0.081	1.6 ± 0.3	11.1 ± 0.1	8.5 ± 8.3	1.8 ± 0.1	10.6 ± 0.1	106 ± 45	0.50 ± 0.37	13	
	0.575 ± 0.096	4.4 ± 0.4	11.3 ± 0.4	43.6 ± 10.2	4.4 ± 0.1	11.6 ± 0.1	111 ± 21	5.46 ± 1.48	13	
	0.186 ± 0.003	3.3 ± 0.1	17.9 ± 0.1	10.9 ± 0.1	3.3 ± 0.1	16.5 ± 0.1	71 ± 8	0.86 ± 0.11	13	
	0.060 ± 0.003	5.2 ± 0.1	25.3 ± 0.1	3.5 ± 0.2	5.8 ± 0.1	25.3 ± 0.1	69 ± 14	0.43 ± 0.09	13	
	0.055 ± 0.002	1.9 ± 0.1	−46.5 ± 0.1	…	…	…	…	…	…	
	0.048 ± 0.003	3.0 ± 0.2	−4.8 ± 0.1	…	…	…	…	…	…	
	0.076 ± 0.003	1.8 ± 0.1	24.6 ± 0.1	…	…	…	…	…	…	
3C410B	0.021 ± 0.002	5.3 ± 0.4	−47.6 ± 0.2	0.8 ± 0.1	5.8 ± 0.1	−52.0 ± 0.1	39 ± 3	0.08 ± 0.01	12	0.0
	0.019 ± 0.002	1.8 ± 0.3	−30.2 ± 0.1	0.4 ± 0.0	2.0 ± 0.1	−30.1 ± 0.1	18 ± 3	0.01 ± 0.00	12	
	0.476 ± 0.007	2.7 ± 0.1	−0.2 ± 0.1	12.2 ± 0.1	2.9 ± 0.1	−0.2 ± 0.1	28 ± 2	0.71 ± 0.07	12	
	0.344 ± 0.023	11.4 ± 0.5	5.1 ± 0.3	46.3 ± 3.5	12.6 ± 0.1	4.6 ± 0.1	153 ± 12	11.71 ± 1.36	1	
	0.292 ± 0.011	1.5 ± 0.1	5.9 ± 0.1	7.5 ± 0.3	1.4 ± 0.1	6.0 ± 0.1	31 ± 3	0.26 ± 0.03	12	
	2.798 ± 0.014	2.2 ± 0.1	8.0 ± 0.1	17.2 ± 0.2	2.4 ± 0.1	8.0 ± 0.1	18 ± 1	2.15 ± 0.24	12	
	0.430 ± 0.137	1.9 ± 0.1	10.9 ± 0.1	22.0 ± 8.4	2.0 ± 0.1	10.2 ± 0.1	65 ± 21	1.06 ± 0.49	12	
	0.041 ± 0.017	19.2 ± 2.0	12.7 ± 3.1	40.7 ± 16.7	19.1 ± 0.1	11.4 ± 0.1	1006 ± 403	15.52 ± 9.16	12	
	0.112 ± 0.004	2.5 ± 0.1	25.2 ± 0.1	3.9 ± 0.1	2.8 ± 0.1	25.1 ± 0.1	32 ± 3	0.18 ± 0.02	12	
	0.426 ± 0.010	2.3 ± 0.1	2.5 ± 0.1	…	…	…	…	…	…	
	0.119 ± 0.005	2.5 ± 0.1	18.4 ± 0.1	…	…	…	…	…	…	
	0.347 ± 0.087	2.6 ± 0.3	12.2 ± 0.4	…	…	…	…	…	…	
B2050	0.007 ± 0.001	3.4 ± 0.2	−21.3 ± 0.1	1.0 ± 0.1	3.7 ± 0.1	−21.2 ± 0.1	141 ± 9	0.06 ± 0.01	9	1.0
	0.011 ± 0.001	2.4 ± 0.1	−11.5 ± 0.1	0.8 ± 0.0	2.7 ± 0.1	−12.5 ± 0.1	78 ± 12	0.04 ± 0.01	9	
	0.043 ± 0.002	10.0 ± 0.3	−0.1 ± 0.2	18.2 ± 1.0	10.0 ± 0.1	−0.1 ± 0.1	453 ± 29	3.79 ± 0.34	9	
	0.039 ± 0.002	2.0 ± 0.1	2.5 ± 0.1	0.6 ± 0.0	2.0 ± 0.1	2.7 ± 0.1	13 ± 5	0.02 ± 0.01	9	
	0.150 ± 0.002	1.7 ± 0.1	9.0 ± 0.1	0.4 ± 0.0	1.7 ± 0.1	8.2 ± 0.1	10 ± 6	0.05 ± 0.03	2	
	0.190 ± 0.002	6.0 ± 0.1	10.2 ± 0.1	21.5 ± 0.3	6.0 ± 0.1	9.4 ± 0.1	142 ± 15	3.16 ± 0.35	1	
	0.074 ± 0.002	3.8 ± 0.1	15.9 ± 0.1	1.7 ± 0.0	4.1 ± 0.1	16.2 ± 0.1	28 ± 6	0.15 ± 0.04	9	
	0.086 ± 0.002	2.8 ± 0.1	−0.8 ± 0.1	…	…	…	…	…	…	
	0.014 ± 0.002	1.2 ± 0.1	−6.1 ± 0.1	…	…	…	…	…	…	
3C433	0.181 ± 0.010	1.5 ± 0.1	2.6 ± 0.1	2.2 ± 0.2	1.6 ± 0.1	2.4 ± 0.1	21 ± 9	0.11 ± 0.05	2	1.0
	0.304 ± 0.009	3.9 ± 0.1	3.5 ± 0.1	19.1 ± 0.7	4.1 ± 0.1	3.5 ± 0.1	78 ± 5	1.82 ± 0.15	1	
	0.080 ± 0.005	2.1 ± 0.1	7.3 ± 0.1	1.8 ± 0.1	2.1 ± 0.1	7.3 ± 0.1	29 ± 5	0.09 ± 0.02	4	
	0.059 ± 0.004	2.5 ± 0.1	16.5 ± 0.1	1.6 ± 0.0	2.7 ± 0.1	15.7 ± 0.1	29 ± 2	0.08 ± 0.01	4	
PKS2127	0.073 ± 0.001	2.7 ± 0.1	−0.9 ± 0.1	7.6 ± 0.1	2.7 ± 0.1	−0.9 ± 0.1	105 ± 4	0.40 ± 0.02	1	1.0
	0.013 ± 0.001	8.3 ± 0.2	1.1 ± 0.1	9.7 ± 0.6	8.3 ± 0.1	1.2 ± 0.1	769 ± 43	1.59 ± 0.14	2	
	0.107 ± 0.001	2.1 ± 0.1	1.5 ± 0.1	5.8 ± 0.1	2.0 ± 0.1	1.5 ± 0.1	61 ± 5	0.27 ± 0.02	3	
J2136	0.096 ± 0.002	2.2 ± 0.1	1.1 ± 0.1	3.1 ± 0.0	2.4 ± 0.1	1.0 ± 0.1	28 ± 3	0.12 ± 0.02	1	0.0
	0.062 ± 0.002	7.0 ± 0.1	3.4 ± 0.1	2.4 ± 0.0	7.7 ± 0.1	3.1 ± 0.1	22 ± 13	0.19 ± 0.12	2	
	0.079 ± 0.002	2.5 ± 0.1	5.8 ± 0.1	7.7 ± 0.1	2.7 ± 0.1	6.3 ± 0.1	98 ± 4	0.37 ± 0.02	3	
J2232	0.066 ± 0.001	2.3 ± 0.1	−14.3 ± 0.1	4.2 ± 0.0	2.5 ± 0.1	−15.0 ± 0.1	65 ± 0	0.19 ± 0.00	5	0.5
	0.056 ± 0.002	2.0 ± 0.1	−7.6 ± 0.1	3.1 ± 0.1	2.0 ± 0.1	−7.6 ± 0.1	58 ± 3	0.13 ± 0.01	5	
	0.064 ± 0.002	5.7 ± 0.1	−5.0 ± 0.1	6.6 ± 0.2	5.7 ± 0.1	−5.0 ± 0.1	105 ± 4	0.75 ± 0.04	5	
	0.099 ± 0.002	2.0 ± 0.1	−3.6 ± 0.1	2.9 ± 0.1	2.1 ± 0.1	−3.6 ± 0.1	32 ± 4	0.12 ± 0.02	5	
	0.046 ± 0.002	3.3 ± 0.1	2.1 ± 0.1	4.3 ± 0.1	3.6 ± 0.1	2.3 ± 0.1	96 ± 3	0.28 ± 0.01	1	
3C454.3	0.313 ± 0.024	2.5 ± 0.1	−10.3 ± 0.1	5.0 ± 0.5	2.8 ± 0.1	−10.6 ± 0.1	20 ± 2	0.31 ± 0.04	1	1.0
	0.025 ± 0.013	3.7 ± 1.2	−8.5 ± 1.3	4.0 ± 2.1	3.7 ± 0.1	−8.1 ± 0.1	159 ± 90	0.28 ± 0.24	8	
	0.096 ± 0.002	3.6 ± 0.1	−2.1 ± 0.1	12.9 ± 0.1	3.6 ± 0.1	−2.1 ± 0.1	142 ± 2	0.95 ± 0.02	8	
	0.081 ± 0.002	1.8 ± 0.1	0.7 ± 0.1	4.6 ± 0.1	1.9 ± 0.1	0.6 ± 0.1	61 ± 3	0.17 ± 0.01	8	
	0.026 ± 0.002	4.7 ± 0.3	3.0 ± 0.2	2.7 ± 0.1	5.1 ± 0.1	3.3 ± 0.1	109 ± 3	0.25 ± 0.02	8	
	0.047 ± 0.002	2.1 ± 0.1	−30.5 ± 0.1	…	…	…	…	…	…	
	0.016 ± 0.002	5.9 ± 0.2	−16.4 ± 0.1	…	…	…	…	…	…	
	0.010 ± 0.002	3.5 ± 0.2	−35.1 ± 0.1	…	…	…	…	…	…	

Table 5
(Continued)

Source (name)	τ_0	Δv_0 (km s^{-1})	v_0 (km s^{-1})	$T_{B,n}$ (K)	$\Delta v_{0,n}$ (km s^{-1})	$v_{0,n}$ (km s^{-1})	T_s (K)	$N(\mathrm{H\ I})_{\mathrm{abs}_2}$ (10^{20} cm^{-2})	$\mathcal{O}$	$\mathcal{F}$
3C459	0.010 ± 0.001	2.8 ± 0.1	−13.2 ± 0.1	0.7 ± 0.0	3.1 ± 0.1	−12.4 ± 0.1	72 ± 2	0.04 ± 0.00	2	1.0
	0.039 ± 0.002	5.2 ± 0.3	−6.2 ± 0.2	14.4 ± 0.8	5.5 ± 0.1	−6.7 ± 0.1	384 ± 22	1.48 ± 0.14	1	
	0.057 ± 0.002	1.9 ± 0.1	0.4 ± 0.1	2.7 ± 0.1	2.0 ± 0.1	0.4 ± 0.1	37 ± 8	0.08 ± 0.02	7	
	0.039 ± 0.003	7.7 ± 0.6	0.8 ± 0.3	18.3 ± 1.4	7.7 ± 0.1	0.7 ± 0.1	478 ± 35	2.79 ± 0.37	7	
	0.088 ± 0.003	2.2 ± 0.1	2.9 ± 0.1	3.5 ± 0.1	2.2 ± 0.1	2.9 ± 0.1	46 ± 6	0.18 ± 0.03	7	
	0.016 ± 0.001	1.4 ± 0.1	7.7 ± 0.1	0.9 ± 0.0	1.6 ± 0.1	7.7 ± 0.1	56 ± 2	0.03 ± 0.00	7	
	0.102 ± 0.003	2.2 ± 0.1	−7.3 ± 0.1	…	…	…	…	…	…	

Note. Cols. (2)–(4): Gaussian parameters fit to H I absorption (Equation (1)). Cols. (5)–(7): Gaussian parameters fit to H I emission (Equations (2)). Col. (8): average spin temperature from all permutations of components with overlap along the LOS (Equations (3), (4)). Col. (9): column density computed from fitted parameters (Equation (6)). Col. (10): order of components along the LOS corresponding to the smallest model residuals. Components whose position along the LOS is extremely uncertain or unaffected by order permutations are assumed to lie behind all others (i.e., $\mathcal{O} = N$, for N total components). Col (11): fraction of WNM (emission-detected only) components that lie in front of all absorption-detected components, allowed to be 1.0 or 0.0 for all emission-detected components. Fit parameters for components with $T_s \leqslant 3$ K are omitted, as these are either spurious AGD detections or were not recovered in the fit to $T_{B,\mathrm{exp}}(v)$ due to strong line blending.

ORCID iDs

Claire E. Murray https://orcid.org/0000-0002-7743-8129
W. M. Goss https://orcid.org/0000-0001-6596-8803
John M. Dickey https://orcid.org/0000-0002-6300-7459
Brian Babler https://orcid.org/0000-0002-6984-5752
Chang-Goo Kim https://orcid.org/0000-0003-2896-3725

References

Astropy Collaboration, Robitaille, T. P., Tollerud, E. J., et al. 2013, A&A, 558, A33
Audit, E., & Hennebelle, P. 2005, A&A, 433, 1
Carilli, C. L., Dwarakanath, K. S., & Goss, W. M. 1998, ApJL, 502, L79
Chengalur, J. N., Kanekar, N., & Roy, N. 2013, MNRAS, 432, 3074
Clark, B. G. 1965, ApJ, 142, 1398
Condon, J. J., Cotton, W. D., Greisen, E. W., et al. 1998, AJ, 115, 1693
Crovisier, J., Kazes, I., & Aubry, D. 1978, A&AS, 32, 205
Dalgarno, A., & McCray, R. A. 1972, ARA&A, 10, 375
Dickey, J. M., & Benson, J. M. 1982, AJ, 87, 278
Dickey, J. M., McClure-Griffiths, N., Gibson, S. J., et al. 2013, PASA, 30, e003
Dickey, J. M., Mebold, U., Stanimirovic, S., & Staveley-Smith, L. 2000, ApJ, 536, 756
Dickey, J. M., Salpeter, E. E., & Terzian, Y. 1977, ApJL, 211, L77
Dickey, J. M., Terzian, Y., & Salpeter, E. E. 1978, ApJS, 36, 77
Draine, B. T. 2011, Physics of the Interstellar and Intergalactic Medium (Princeton, NJ: Princeton Univ. Press)
Dwarakanath, K. S., Carilli, C. L., & Goss, W. M. 2002, ApJ, 567, 940
Ewen, H. I., & Purcell, E. M. 1951, Natur, 168, 356
Ferrière, K. M., Zweibel, E. G., & Shull, J. M. 1988, ApJ, 332, 984
Field, G. B. 1958, PIRE, 46, 240
Fukui, Y., Torii, K., Onishi, T., et al. 2015, ApJ, 798, 6
Greisen, E. W. 2003, ASSL, 285, 109
Hagen, J. P., Lilley, A. E., & McClain, E. F. 1955, ApJ, 122, 361
Hartmann, D., & Burton, W. B. 1997, Atlas of Galactic Neutral Hydrogen (Cambridge: Cambridge Univ. Press)
Haud, U., & Kalberla, P. M. W. 2007, A&A, 466, 555
Heiles, C., & Troland, T. H. 2003a, ApJS, 145, 329
Heiles, C., & Troland, T. H. 2003b, ApJ, 586, 1067
Hughes, M. P., Thompson, A. R., & Colvin, R. S. 1971, ApJS, 23, 323
Hunter, J. D. 2007, CSE, 9, 90
Kalberla, P. M. W., Burton, W. B., Hartmann, D., et al. 2005, A&A, 440, 775
Kalberla, P. M. W., & Haud, U. 2015, A&A, 578, A78
Kalberla, P. M. W., & Haud, U. 2018, arXiv:1806.04085
Kalberla, P. M. W., McClure-Griffiths, N. M., Pisano, D. J., et al. 2010, A&A, 521, A17
Kim, C.-G., Ostriker, E. C., & Kim, W.-T. 2013, ApJ, 776, 1
Kim, C.-G., Ostriker, E. C., & Kim, W.-T. 2014, ApJ, 786, 64
Lazareff, B. 1975, A&A, 42, 25
Lee, M.-Y., Stanimirović, S., Murray, C. E., Heiles, C., & Miller, J. 2015, ApJ, 809, 56
Lindner, R. R., Vera-Ciro, C., Murray, C. E., et al. 2015, AJ, 149, 138
Liszt, H. 2001, A&A, 371, 698
Mac Low, M.-M., Balsara, D. S., Kim, J., & de Avillez, M. A. 2005, ApJ, 626, 864
McClure-Griffiths, N. M., Pisano, D. J., Calabretta, M. R., et al. 2009, ApJS, 181, 398
McClure-Griffiths, N. M., Stanimirovic, S., Murray, C., et al. 2015, in Advancing Astrophysics with the Square Kilometre Array (AASKA14), The Hydrogen Universe (Trieste: SISSA), 130
McKee, C. F., & Ostriker, J. P. 1977, ApJ, 218, 148
Mebold, U., Düsterberg, C., Dickey, J. M., Staveley-Smith, L., & Kalberla, P. 1997, ApJL, 490, L65
Mohan, R., Dwarakanath, K. S., & Srinivasan, G. 2004, JApA, 25, 185
Muller, C. A., & Oort, J. H. 1951, Natur, 168, 357
Murray, C. E., Lindner, R. R., Stanimirović, S., et al. 2014, ApJL, 781, L41
Murray, C. E., Peek, J. E. G., Lee, M.-Y., & Stanimirovic, S. 2018, arXiv:1806.01300
Murray, C. E., Stanimirović, S., Goss, W. M., et al. 2015, ApJ, 804, 89
Murray, C. E., Stanimirović, S., Kim, C.-G., et al. 2017, ApJ, 837, 55
Nguyen, H., Dawson, J. R., Miville-Deschênes, M.-A., et al. 2018, arXiv:1805.11787
Peek, J. E. G., Babler, B. L., Zheng, Y., et al. 2018, ApJS, 234, 2
Peek, J. E. G., Heiles, C., Douglas, K. A., et al. 2011, ApJS, 194, 20
Planck Collaboration, Abergel, A., Ade, P. A. R., et al. 2014, A&A, 571, A11
Pritchard, J. R., & Loeb, A. 2012, RPPh, 75, 086901
Radhakrishnan, V., Murray, J. D., Lockhart, P., & Whittle, R. P. J. 1972, ApJS, 24, 15
Reach, W. T., Heiles, C., & Bernard, J.-P. 2017, ApJ, 834, 63
Rohlfs, K., & Wilson, T. L. 2004, Tools of Radio Astronomy (Berlin: Springer)
Roy, N., Kanekar, N., Braun, R., & Chengalur, J. N. 2013a, MNRAS, 436, 2325
Roy, N., Kanekar, N., & Chengalur, J. N. 2013b, MNRAS, 436, 2366
Shaw, G., Ferland, G. J., & Hubeny, I. 2017, ApJ, 843, 149
Stanimirović, S., & Heiles, C. 2005, ApJ, 631, 371
Stanimirović, S., Murray, C. E., Lee, M.-Y., Heiles, C., & Miller, J. 2014, ApJ, 793, 132
Van Der Walt, S., Colbert, S. C., & Varoquaux, G. 2011, CSE, 13, 22
Vázquez-Semadeni, E., Gazol, A., & Scalo, J. 2000, ApJ, 540, 271
Verschuur, G. L., & Magnani, L. 1994, AJ, 107, 287
Vishniac, E. T., & Lazarian, A. 1999, ApJ, 511, 193
Winkel, B., Kerp, J., Flöer, L., et al. 2016, A&A, 585, A41
Wolfire, M. G. 2015, HiA, 16, 600
Wolfire, M. G., McKee, C. F., Hollenbach, D., & Tielens, A. G. G. M. 2003, ApJ, 587, 278
Wouthuysen, S. A. 1952, AJ, 57, 31